ATOMIC LUMINESCENCE INDUCED BY COULOMB EXPLOSION IN A SILICON METAL-OXIDE-SEMICONDUCTOR STRUCTURE

by

Sung Jun Yoon

B.E. in Electrical Engineering, Handong University, 2006

Submitted to the Graduate Faculty of

Swanson School of Engineering in partial fulfillment

of the requirements for the degree of

Master of Science

University of Pittsburgh

2008

UNIVERSITY OF PITTSBURGH

SWANSON SCHOOL OF ENGINEERING

This thesis was presented

by

Sung Jun Yoon

It was defended on

June16, 2008

and approved by

Joel Falk, PhD, Professor, Electrical and Computer Engineering Department

Mahmoud El Nokali, PhD, Associate Professor, Electrical and Computer Engineering Department

Guangyong Li, PhD, Assistant Professor, Electrical and Computer Engineering Department

Thesis Advisor: Hong Koo Kim, PhD, Professor, Electrical and Computer Engineering Department

ATOMIC LUMINESCENCE INDUCED BY COULOMB EXPLOSION IN A SILICON METAL-OXIDE-SEMICONDUCTOR STRUCTURE

Sung Jun Yoon, M.S.

University of Pittsburgh, 2008

The Coulomb fragmentation phenomenon has been known to occur in matter at various different length scales, such as nuclei and atomic or molecular clusters, and microscopic droplets. In many cases, the Coulomb explosion is triggered by sudden ionization with high-intensity ($\geq 10^{14}$ W/cm^2) femto-second laser pulses. At this intensity level, the valence electrons are quickly ripped off and the ionized metal clusters fragment before thermalization occurs.

In this thesis, we report Coulomb explosion of Ag atoms induced by electron impact ionization in a Si metal-oxide-semiconductor (MOS) structure (Ag/SiO_2/Si). Under positive voltage pulses applied to the Ag gate, kinetic electrons are injected onto the gate through leakage channels formed in oxide and impact-ionize the metal atoms at the gate/dielectric interface. When the Coulomb repulsion among the ions becomes stronger than the binding force of metal atoms, the ions accumulated at the interface explode, atomizing the metal and also adjacent dielectrics. This explosive fragmentation results in atomic luminescence from neutral silver at 328 nm, 338 nm, 521 nm, 547 nm, 769 nm, and 827 nm. The mechanisms of oxide breakdown, localized injection of kinetic electrons, and atomization/luminescence are discussed.

TABLE OF CONTENTS

LIST OF TABLES

LIST OF FIGURES

PREFACE

I want to thank Prof. Hong Koo Kim, my advisor, for providing me this tremendous chance to work in his lab. During the time I've spent with him, I have obtained invaluable knowledge from research philosophy to scientific information. I am more than confident that all I have learned from him will be a firm foundation of my future work.

I thank Professors, Joel Falk, Mahmoud El Nokali, and Guangyong Li for taking their busy time to serve on my committee and providing their comments and criticism on my thesis.

I'd like to acknowledge Yun-Suk Jung and Dr. Tae bong Hur for their dedication to help me to learn all experimental works. Moreover, their advice and encouragement are unforgettable.

My greatest thanks should go to my parents. Their unfailing trust and love to their only child bring him to leave them for his dream, but in the deepest place of his heart, they have been always with him and forever will be.

Lastly, but to the greatest, the one who showed me his love by his death, I send all my thanks and glory.

1.0 INTRODUCTION

1.1 OVERVIEW

The Coulomb fragmentation phenomenon has been known to occur in matter at various different length scales, such as nuclei and atomic or molecular clusters, and microscopic droplets [1-7]. Nuclear fission or fragmentation was discovered in early 1900s [1]. Recent development of ultrafast high intensity laser system enabled the production of hot (~1 keV), highly ionized plasmas by intense irradiation of solids or gases with high-intensity ($\geq 10^{14}$ W/cm^2) femto-second laser pulses [4]. At this intensity level (> 3VÅ^{-1}), the laser field exceeds the Coulombic field strength seen by an electron in the core states of an atom [3]. The valence/core electrons are quickly ripped off and the ionized metal clusters fragment before thermalization occurs. In an alternative experiment designed for Coulomb explosion, highly kinetic ions (~MeV) impinged upon metal clusters inducing ionization of metal atoms [8].

In this thesis, we report Coulomb explosion of Ag atoms induced by electron impact ionization in a Si metal-oxide-semiconductor (MOS) structure (Ag/SiO_2/Si). Under positive voltage pulses applied to the Ag gate, kinetic electrons are injected onto the gate through leakage channels formed in oxide and impact-ionize the metal atoms at the gate/dielectric interface. When the Coulomb repulsion among the ions becomes stronger than the binding force of metal

atoms, the ions accumulated at the interface explode, atomizing the metal and also adjacent dielectrics.

This explosive fragmentation results in atomic luminescence from neutral silver (Ag I) at 328 nm ($^2P_{3/2}$ - $^2S_{1/2}$), 338 nm ($^2P_{1/2}$ - $^2S_{1/2}$), 521 nm ($^2D_{3/2}$ – $^2P_{1/2}$), 547 nm ($^2D_{5/2}$ – $^2P_{3/2}$), 769 nm ($^2S_{1/2}$ - $^2P_{1/2}$), and 827 nm ($^2S_{1/2}$ - $^2P_{3/2}$) [9-11]. Atomic luminescence from silicon (Si I at 252 nm and Si II at 590 nm) and neutral oxygen (O I at 778 nm) is also observed. The mechanisms of oxide breakdown, localized injection of kinetic electrons, and atomization/luminescence are discussed.

1.2 CURRENT TRANSPORT IN METAL-OXIDE-SEMICONDUCTOR STRUCTURE

To accommodate readers' understanding of the phenomena that will be discussed in this thesis, it is necessary to deal with the background information prior to the main discussion. First, the mechanisms of current transport through oxide and an accompanying oxide breakdown in a MOS structure will be discussed. Fundamental understanding of Coulomb explosion will be followed. Lastly, atomic luminescence will be covered.

Ideally, an insulator does not allow charges to conduct through itself. In practice, however, there is a leakage current, when the electric field or temperature is decently high. For the Si-SiO_2 structure, the avalanche breakdown field in silicon is about $3x10^5$ V/cm; accordingly the field in the oxide is about three times larger, ~10^6 V/cm by $\varepsilon_{Si} / \varepsilon_{ox} = 11.7 / 3.9$. At this level of electric field, conduction by hole or electron in SiO_2 is trifling. However, for ultra-thin SiO_2 with high electric field, tunneling may occur. Figures 1.1 and 3.2 illustrate the band diagram of a MOS structure under gate voltage. There is a potential barrier, which blocks electrons from passing through the oxide. Classically, it is impossible for electrons to pass through the barrier when the energy of electron is lower than the barrier height. However, in quantum mechanics, there is some possibility of tunneling through the barrier, eventually conducting through the oxide layer, if the barrier layer is sufficiently thin. We will discuss two of the mechanisms of current transport by tunneling; Fowler-Nordheim tunneling and direct tunneling [12,13,16,17,18].

In Si based metal-oxide-semiconductor (MOS) structures, the gate leakage currents are mainly due to Fowler-Nordheim (FN) tunneling or direct tunneling as shown in Figure 1.1. For

the oxide with thickness below 4 nm, direct tunneling, as shown in figure 1.1(b), dominates the leakage mechanism. However, for sufficiently thick gate dielectric films (> 4 nm), the leakage current is dominated by FN tunneling, as shown in Figure 1.1(a) [14].

In Fowler-Nordheim tunneling, electrons from the Si conduction band hop into the conduction band of SiO_2. By solving Schrodinger equation, the current density through SiO_2 can be expressed as Eq.(1)

$$\frac{J_{FN}}{E_{ox}^2} = A\exp\left(\frac{-B}{E_{ox}}\right) \quad \text{.....(1)}$$

$$A = \frac{e^3 m}{16\pi^2 \hbar m_{ox} \phi_0},\ B = \frac{4}{3}\frac{(2m_{ox})^{1/2}}{e\hbar}\phi_0^{3/2}$$

where E_{ox} is the electric field in the gate oxide, and e is the electron charge, m is the free space electron mass, m_{ox} is the effective mass of electron in the oxide, $2\pi\hbar$ is the Planck constant, and ϕ_0 is the barrier height in eV. A plot of $\ln\left(J/\varepsilon_{ox}^2\right)$ vs $1/E$ called the FN plot gives the value of constant B, as is shown in Figure1.2 [14].

As the gate oxide becomes thinner, the tunneling barrier in the gate oxide also becomes thin so that the electrons in the conduction band of Si can tunnel through the gate oxide and emerge in the gate, without having to go via the conduction band of the gate oxide. This is known as direct tunneling rather than Fowler-Nordheim tunneling. Eq. (2) is an expression of the current density of direct tunneling [15].

$$J_{DT} = AE_{ox}^2 \left(\frac{\phi_0}{V_{ox}}\right)\left(\frac{2\phi_0}{V_{ox}} - 1\right)\exp\left(\frac{-B\left(1-\left(1-\frac{V_{ox}}{\phi_0}\right)^{3/2}\right)}{E_{ox}}\right), \text{ when } V_{ox} > 1V$$

$$J_{DT} = AE_{ox}^2 \exp\left(\frac{-B\left(1-\left(1-\frac{V_{ox}}{\phi_0}\right)^{3/2}\right)}{E_{ox}}\right), \text{ when } V_{ox} < 1V \quad \ldots\ldots\ldots\ldots\ldots(2)$$

It should be noted that both Fowler-Nordheim and direct tunneling are based on the assumption that the oxide is defect free.

However, if the oxide layer is deposited by sputtering, there should be a number of defects. In that case, the most appropriate tunneling model will be Poole-Frenkel tunneling. The structural defects cause additional energy states close to the band edge, called traps. These traps restrict the current flow because of a capture and emission process, thereby becoming the dominant current transport mechanism [26,27].

$$J_{PF} = en_0\mu E_{ox} \exp\left(-\frac{e}{kT}\left(\phi_0 - \sqrt{\frac{eE_{ox}}{\pi\varepsilon}}\right)\right) \quad \ldots\ldots\ldots\ldots..(3)$$

Both the Fowler-Nordheim tunneling and the Poole-Frenkel emission mechanisms produce very low current densities. If, in a structure, carriers can readily enter the insulator and freely flow through the insulator, then the resulting current and carrier densities could be much higher. The high density of charge carriers in insulator induces a field gradient, which can

adversely affect further injection of current. In another words, when the energy barriers at the contacts become negligible, and when trapping of injected carriers at localized energy levels is not involved, then it is possible to reach a much higher level of current, limited by space charges, so-called a space charge limited current[19,29].

When the insulator is a vacuum, specifically, this current transport is called as the Child space-charge-limited current. In the Child space-charge-limited current, carriers are supposed to be transported ballistically without scattering. This implies carriers can be accelerated significantly by the electric field inside the insulator.

C. D. Child and I. Langmuir, for the first time, introduced the space-charge-limited current model to estimate the current flow between two infinitely parallel plates in a vacuum when voltage is applied between the two plates [20,21]. Let us assume that plate 'A' is connected to the ground and plate 'B' is positively charged. If the temperature at plate 'A' is significantly low, no electrons are supposed to be emitted from the plate 'A', which means that the voltage in the middle of the two plates will be linear. As the temperature at plate 'A' is increased, electrons will be given off from the plate 'A'. The released electrons comprise a current with magnitude i. If we start with a rough assumption that the velocity of electrons in between the two plates is constant, space charge will also be uniform by the Eq. (4) and it follows the Laplace's equation like the Eq. (5).

$$i = \rho v \quad \text{.....(4)}$$

$$\Delta V = \frac{d^2V}{dx^2} + \frac{d^2V}{dy^2} + \frac{d^2V}{dz^2} = -4\pi\rho \quad \text{.....(5)}$$

If the current is increased further, potential will be parabolic according to the Eq. (5), but at some point, the potential curve will be normal to the surface of the plate 'A'. In other words, the initial velocity of electrons is zero, since there will be no dragging force for electrons to be accelerated at near the surface of the plate 'A'. If the current is increased further, a negative potential will be built up, so that the electrons may feel a barrier when they come out from the plate 'A'. Even more, the electrons are so slow that they can hardly overcome the barrier. To sum up, space-charge limits the current increase after a certain level, so that further increase of temperature of the plate 'A' will make current increase no longer.

Our interest is in the current-voltage relationship before current saturation. Let us say that V is the potential at a distance x from the plate 'A'. Then, the kinetic energy of an electron that travels for distance x from the plate 'A' can be expressed as Eq. (6).

$$\frac{1}{2}mv^2 = Ve \quad \text{.....(6)}$$

Eq. (5) can evolve to Eq(8), when we say that the e or ρ is positive number even for electrons.

$$\frac{d^2V}{dx^2} = 4\pi\rho \quad \text{.....(7)}$$

By Eq. (4), ρ can be replaced by i/v, and v can be substituted by $\sqrt{\frac{2eV}{m}}$.

$$\frac{d^2V}{dx^2} = 2\pi\sqrt{2}\sqrt{\frac{m}{e}}\frac{i}{\sqrt{V}} \quad \text{.....(8)}$$

Multiplying both sides of Eq. (8) by $2\frac{dV}{dx}$ and integrating it respect to x will produce Eq. (9)

$$\left(\frac{dV}{dx}\right)^2 - \left(\frac{dV}{dx}\right)_0^2 = 8\pi i\sqrt{\frac{2mV}{e}} \quad \text{.....(9)}$$

Reminding that the potential gradient at the plate 'A' is zero, Eq. (9) becomes Eq. (10)

$$\frac{dV}{dx} = \sqrt{8\pi i}\sqrt[4]{\frac{2mV}{e}} \quad \text{.....(10)}$$

Integrating and solving for i, finally the current-voltage relationship will be like Eq. (11)

$$i = \frac{\sqrt{2}}{9\pi}\sqrt{\frac{e}{m}}\frac{V^{\frac{3}{2}}}{x^2} \quad \text{.....(11)}$$

The Child space-charge-limited current can be expressed in terms of current density and voltage as Eq. 12 [20, 28].

$$J_{Child-SCLC} = \frac{4\varepsilon}{9}\sqrt{\frac{2e}{m}}\frac{V_{ox}^{3/2}}{d^2} \quad \text{.....(12)}$$

On the other hand, when the insulator is a solid, so that there are dense blockages on the path of carriers, the transport mechanism is different from the Child space-charge-limited current.

This mechanism is the Mott-Gurney space-charge-limited current. Highly kinetic carriers cannot be generated because of collisions with atoms. The current-voltage relation in the Mott-Gurney space-charge-limited current is in Eq. 13 [28].

$$J_{Mott-Gurney-SCLC} = \frac{9\varepsilon\mu V_{ox}^{\ 2}}{8d^{3}} \quad \text{.....(13)}$$

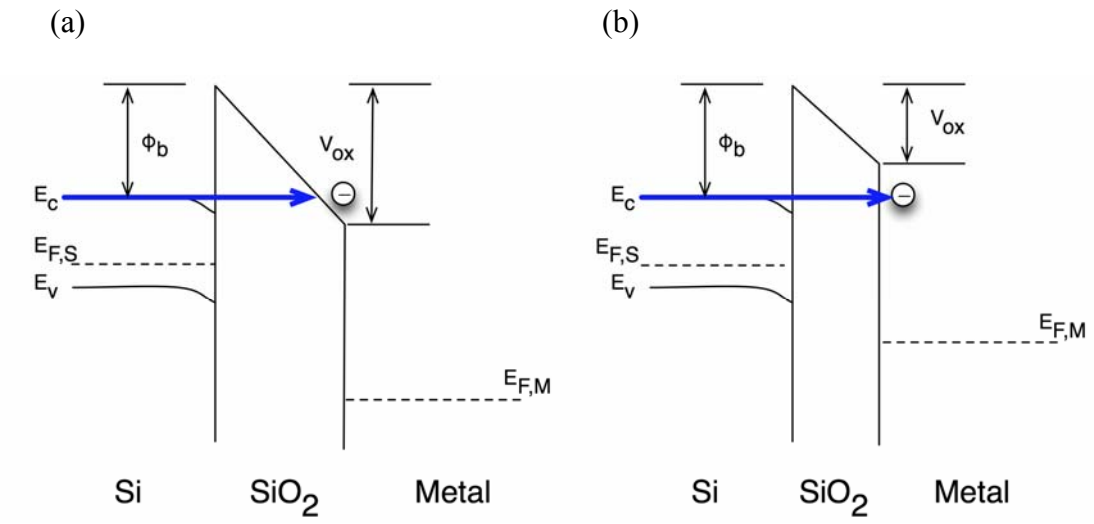

Figure 1.1 (a) Fowler-Nordheim tunneling, (b) Direct tunneling [15]

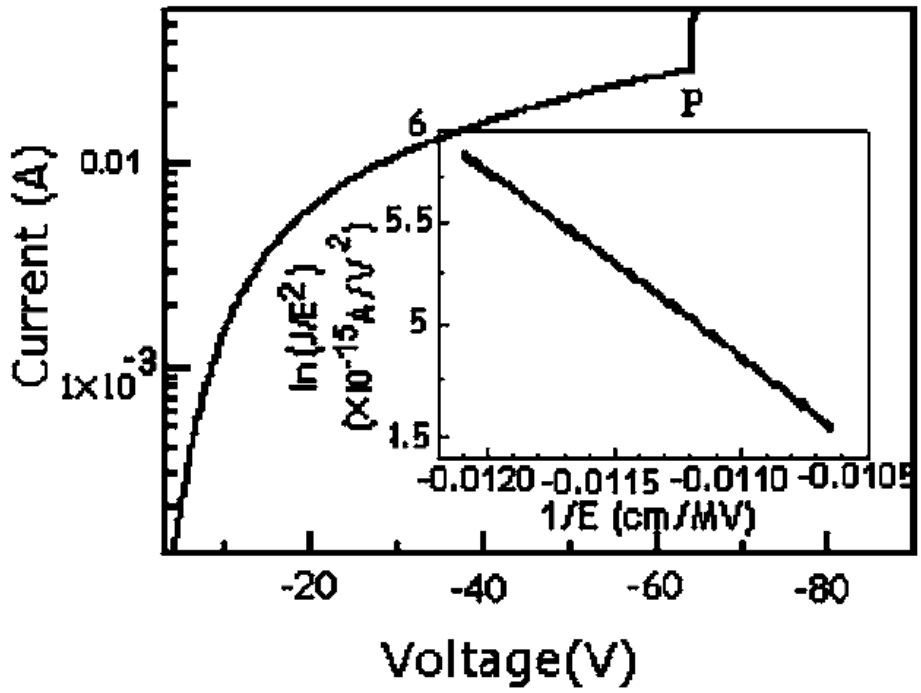

Figure 1.2 *I-V* characteristics of Fowler-Nordheim tunneling transport with the structure Pt–Er_2O_3-silicon measured at 77 K. [14]

1.3 OXIDE BREAKDOWN PROCESS IN METAL-OXIDE-SEMICONDUCTOR STRUCTURE

One of the most important reliability problems of modern integrated circuits is the breakdown of the thin gate oxide. It has been known that there is a relationship between the breakdown at low fields and macroscopic defects (e.g. as particulate, oxide thinning, stacking faults, etc). By improvement of materials processing and device fabrication technology, this issue has been greatly improved. However, the breakdown at high fields is an intrinsic phenomenon, and is usually coupled to defects of microscopic or low-dimensional structures. Several mechanisms, involving hot electrons with energy between 2 and 9 eV, have been reported, that can explain the formation of oxide defects. It should be noted that the energy required for band gap impact ionization is about 9 eV, for anode hole injection, about 5 eV, and for trap creation, about 2 eV. For oxide with above 10 nm thickness, electrons can have average energies of about 6 eV at fields of 8~12 MV/cm, when they are injected from cathode into the oxide conduction band and stabilized into a steady-state conduction. In the case of oxides with less than 10 nm thickness, electrons are known to be ballistic [24].

It has been reported that breakdown occurs after oxide degradation, when a critical density of electron traps are created in the oxide. In other words, the breakdown is a collective formation of leakage paths between anode and cathode, caused by defects of size of the order of 1 nm. Accordingly, we can consider the intrinsic dielectric breakdown as a three stage process, as it is shown in Figure 1.3; the wearout phase, the breakdown, and the thermal damage phase caused by the energy dissipation in the MOS structure. Especially, the thermal damage is also

called as hard breakdown. Without the third stage, thermal damage, the breakdown is described as soft breakdown. Particularly, the soft breakdown can be observed from thin oxides or under stresses with low current flow, showing a few leakage paths without thermal damage in the MOS capacitor [24].

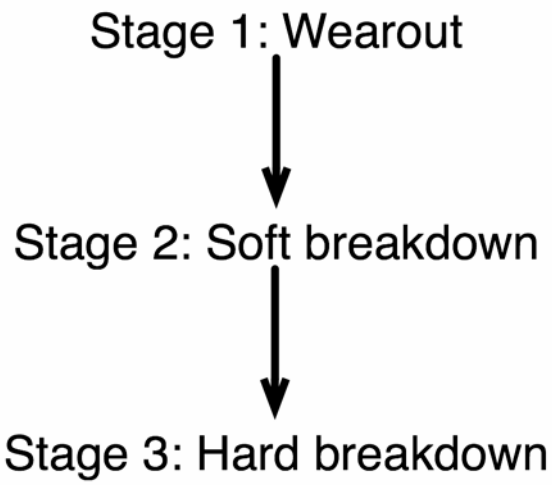

Figure 1.3 Oxide breakdown 3 stage process [24]

1.4 COULOMB EXPLOSION

Coulomb explosion is a process in which a cluster of various sizes is fragmented into smaller pieces by Coulomb repulsion force. To induce Coulomb repulsion force, a cluster should go through a charging event by external source. Initial charging sources for Coulomb explosion are mainly high intensity laser fields or interaction with highly charged ion. Once a system is charged, size of the system affects the efficiency of Coulomb explosion. Small systems are easily fragmentized, since the charges inside the system can sufficiently build up. This is because the distance between charged ions are closer compared to the case of a larger system, which implies Coulomb force is stronger when distance is short by $F \propto \frac{q_1 q_2}{d^2}$.

Instability of highly charged objects was observed frequently, but poorly understood until Lord Rayleigh's original idea was introduced. Lord Rayleigh, in his paper (1882)[47], proved that a spherical shape droplet of radius a_0, surface tensions σ and charge Q, stays stable unless the fissility (X) exceeds unity.

$$X = \frac{Q^2}{64\pi^2 \varepsilon_0 \sigma a_0^3} \quad \text{.....(14)}$$

As X approaches unity, the droplet deformation starts and begins to be unstable. However when X increases beyond unity, an unbalanced state occurs, which causes the formation of fine jets (known as Rayleigh jets) [6].

Coulomb fragmentation is often stimulated by rapid ionization via an ultra-fast laser with high intensity. The ionization process has become available with high peak power, femto-second lasers, which have capacity of generating focused light intensity up to $10^{14} \sim 10^{19}$ W·cm^{-2}. The required intensity for ionization by multiphoton absorption was formulated in the Keldysh theory[48].

When moderate intensities are applied, the normal multi-photon excitation route for ionization via intermediate states applies (see Figure 1.4(*a*)). If the incident field intensity is high enough and the frequency is low enough, the field will distort the atomic potential, so that a potential barrier can be formed through which the electron can tunnel within a quasi-stationary approximation. Figure 1.4(*b*) illustrates the procedure. As the field strength is increased, the field gradient becomes more negative, which implies that the potential barrier becomes smaller and eventually the ground state is not bound anymore. For the ground state of hydrogen case, 1.4x10^{14} W·cm^{-2} of high intensity field is required with low frequency in order to achieve potential barrier elimination with external field. This is known as over-the-barrier ionization (OTBI) (Figure 1.4(*c*)) [30].

For the calculation of required field intensity and frequency, first a parameter γ should be defined in terms of the ratio of the field-free ionization energy U_I of an atom to the quiver energy U_Q of a free electron oscillating in the laser field. Tunneling is dominant if the condition below is met.

$$\gamma = \left(\frac{U_I}{2U_Q} \right)^{1/2} << 1 \quad \text{.....(15)}$$

(Ilkov ***et al.*** [25] have shown a more practical limit for tunneling of $\gamma << 0.5$)

The quiver energy is dependent on the laser angular frequency ω and the amplitude E of the electric field:

$$U_Q = \frac{e^2 E^2}{4 m_e \omega^2} \text{ ……..……..(16)}$$

where e and m_e are the charge and mass of the electron, respectively. The equation clearly shows that the tunneling regime is plausible with low frequencies and high intensities [3].

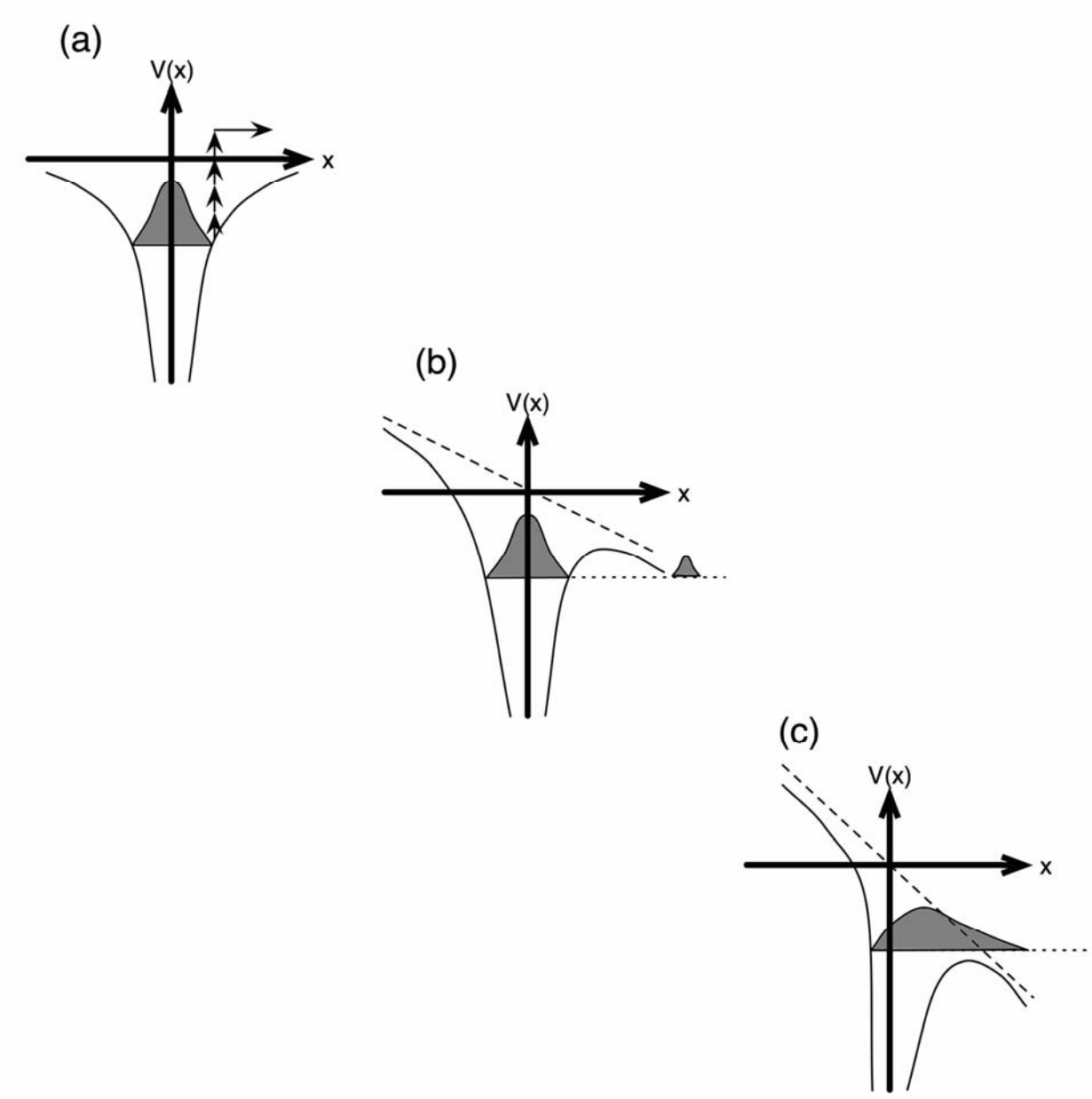

Figure 1.4 (a) Ionization by multi-photon excitation $I < 10^{14}$ Wcm^{-2},

(b) Ionization by tunneling $I < 10^{15}$ Wcm^{-2}, (c) Ionization over the barrier $I > 10^{15}$ Wcm^{-2} [30]

1.5 ATOMIC LUMINESCENCE

Ernest Rutherford is the first who proposed a planetary model for atoms in 1911, as it is called Rutherford model. According to his model, however, electron orbiting around nucleus would gradually spiral inward as it loses energy by electromagnetic radiation, which is unrealistic in the sense that all matter should be unstable. Two years later, Niels Bohr proposed that electrons travel in circular orbits and that only certain orbits are allowed. This model, so-called 'Bohr's model of atoms, opened up a new era of quantum mechanics.

According to Bohr's model, electrons move around a nucleus along a circular orbital, which has quantized angular momenta. Moreover, electron has certain energy, when it travels in an orbit. It only loses or gains energy by jumping up or down to another orbit. Loss or gain of energy of electron indicates emission or absorption of electromagnetic radiation with a frequency ν by Eq. (17)

$$E_2 - E_1 = h\nu \text{ ……..……..(17)}$$

The Rydberg formula illustrates the relation between the transition of orbits and wavelength of the consequent electromagnetic radiation.

$$\Delta E = E_i - E_f = R_E\left(\frac{1}{n_f^2} - \frac{1}{n_i^2}\right) = \frac{hc}{\lambda} \text{ ……....(18)}$$

$$\text{or } \frac{1}{\lambda} = R\left(\frac{1}{n_f^2} - \frac{1}{n_i^2}\right) \text{…….....(19)}$$

Where n_f is the final energy level, and n_i is the initial energy level, and R_E is the Rydberg's constant and $R = R_E / hc$ [22].

For example, the atomic spectrum of hydrogen atom is shown in Figure 1.5. Transition from one orbit to another emits or absorbs photons with wavelength determined from Rydberg formula. According to the final energy level n_f, spectrum is categorized as Lyman, Balmer, Paschen, Brackett, and Pfund series, where each corresponds to n_f = 1, 2, 3, 4, 5, respectively.

Atomic spectrum can be acquired with a special experimental setup to atomize, excite, and measure very narrow atomic lines. First of all, the sample must be converted to free atoms, usually in a high-temperature excitation source. Liquid samples are nebulized and carried into the excitation source by a flowing gas. Solid samples can be introduced into the source by a slurry or by laser ablation of the solid sample in a gas stream. The excitation source must atomize, and excite the analyte atoms. Next, atomic emission should be analyzed with a high-resolution polychromator to selectively monitor each emission line, since the atomic emission lines are very narrow.

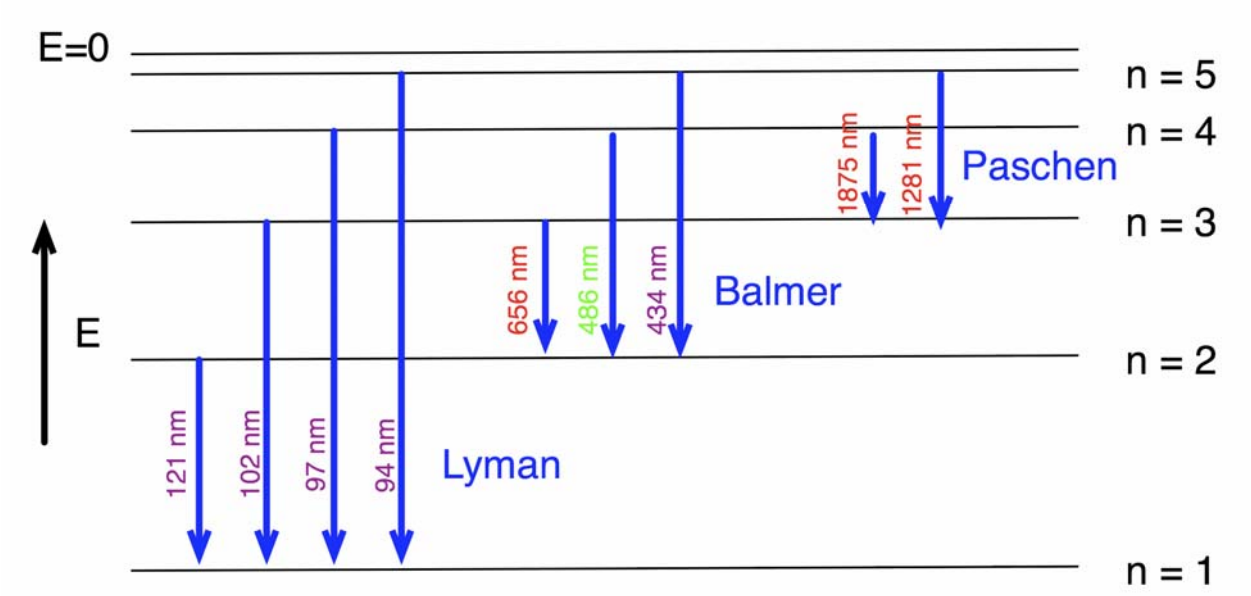

Figure 1.5 A schematic of electron transitions in a hydrogen atom [12]

2.0 FABRICATION

The oxide thickness of a MOS device has continuously decreased as the device size scales down with the Moore's law. This scaling has increased the level of integration and the operating speed of circuits. However, degradation of computational reliability and increase of power consumption caused by 'off-state' leakage current have become a serious issue. In this thesis, we have investigated a MOS structure with oxide thickness in the range of 5-10 nm, which corresponds to the state-of-the-art MOS technology. As shown in Figure 3.1, our typical structure is 15 nm Ag/5-10 nm SiO2/p-type Si. The MOS capacitor structure was formed on p-type Si [(100)-oriented; B doped; 5~15 Ohm-cm resistivity] or n-type Si [(100)-oriented; P doped; 5~30 Ohm-cm resistivity] wafers using a standard Si process. On the silicon substrate, a thermally grown SiO_2 layer was added. After that, an Al layer was deposited on the backside for electrical contact of the substrate. Finally a front side metal layer was deposited. In this chapter, we will discuss the fabrication process of the structure with a thin oxide layer and a thin front metal layer

2.1 OXIDE GROWTH

In this study, it is critical to form a thin oxide layer in order to achieve impact ionization of metal atoms at moderate voltages. For precise control of oxide thickness, calibration of furnace temperature was performed prior to oxide growth.

We first removed native oxide on substrate using the RCA cleaning process. After the native oxide removal, samples were placed in a furnace (Thermco, MB-71), which was set to 850-ºC. Each sample was taken out after 0.5 hr, 1 hr, 1.5 hr, 2 hr, 2.5 hr, and 3 hr. After oxide growth, step-etching was performed on the samples by photo-lithography + chemical etching. The thickness was measured with a surface profiler (KLA Tencor, Alpha-Step IQ). From the experimental data, the following relationship is established between oxide thickness and oxidation time at the given temperature (850 ºC).

$$Thickness[nm] = 13.758 \times (Time[hr])^{0.5685} \quad \text{.....(20)}$$

According to the growth curve equation (Eq. 20), 34 min of oxidation produces 10 nm thick oxide. The surface profiler measurement was compared with a spectroscopic ellipsometer (Horiba Jobin Yvon, UVISEL) measurement, and the two showed a reasonably good agreement (e.g., 10 nm vs 8.5 nm).

After oxidation of silicon substrate, to make an ohmic contact, the backside was deposited with a 150-nm-thick Al (Alfa Aesar, 5N purity) by thermal evaporation deposition. Before Al deposition, the grown oxide on the backside was removed by etching with

BHF(H_2O:HF=4:1), while protecting the front side oxide layer with a photoresist layer. After Al layer deposition, the front side protective photoresist layer was removed and the specimen was annealed in a furnace (350 ºC) in N_2 ambient for 30 min. To check whether ohmic contact was established, contact resistance was measured. Al dots were deposited through a 0.73-mm-diameter hole shadow mask (each dot spacing is 1.73 mm from center to center). I-V characteristic was measured for varying distances between dots. Contact resistance was calculated by Transfer Length Method (TLM). It was confirmed that an ohmic contact between Si substrate and the Al layer was defined.

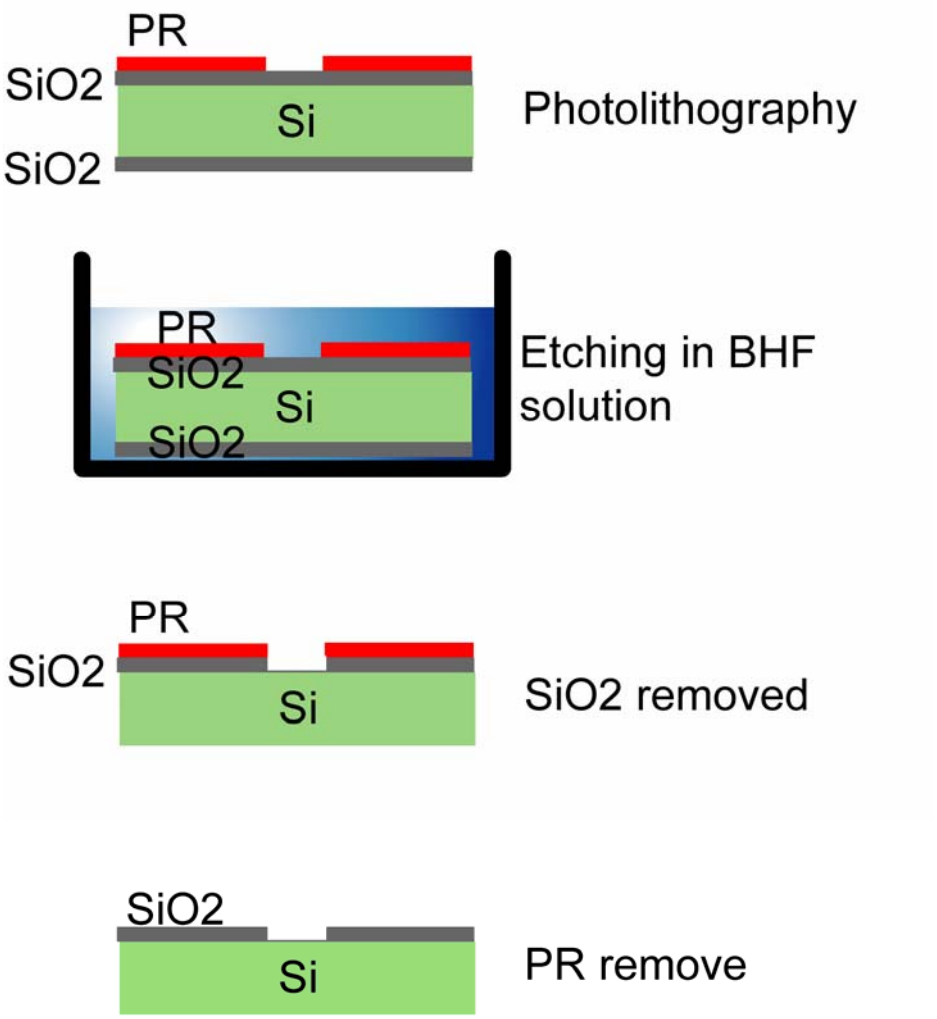

Figure 2.1 Step-etching of front side SiO_2 layer and complete removal of backside SiO_2

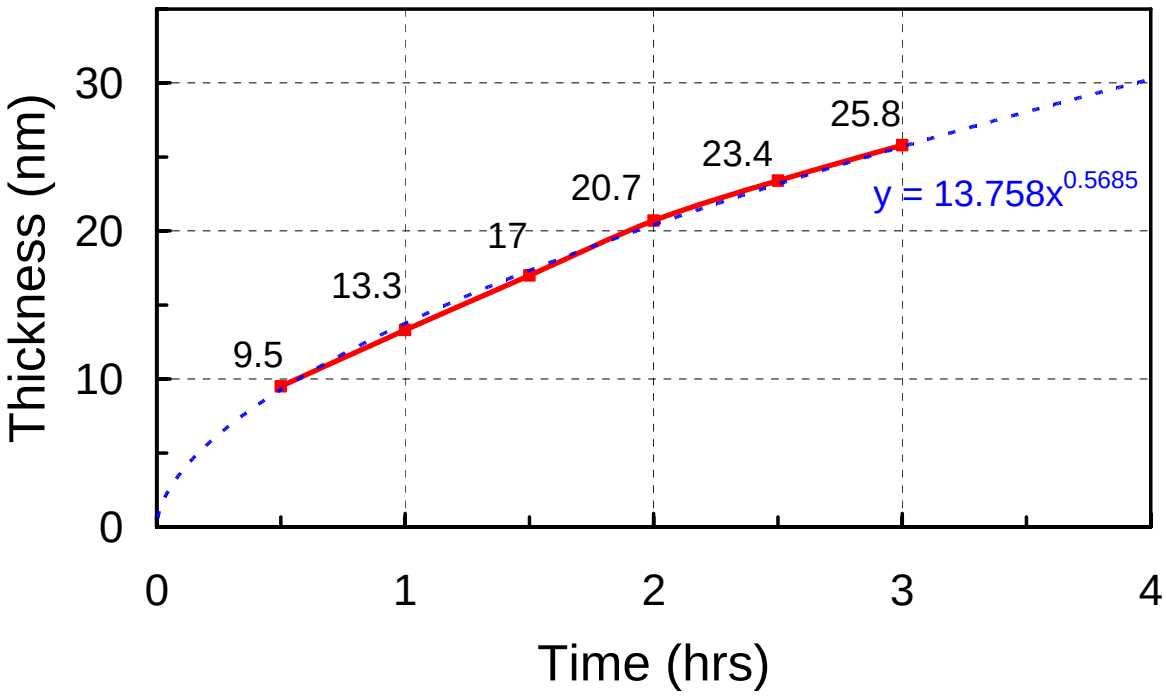

Figure 2.2 Thermally grown SiO_2 growth rate curve at 850 ºC in air ambient. Sample: p-type Si [(100)-oriented; B doped; 5~15 Ohm-cm resistivity]

2.2 THIN FILM DEPOSITION

The front side electrode was deposited by thermal evaporation and/or RF magnetron sputtering deposition. For the case of Ag, Al, and Au, thermal evaporation was used. For the case of Pt, RF magnetron sputtering was used. A shadow mask was used to define an array of electrode dots.

For thermal evaporation of metal (Ag, Al, Au), first, a metal source was placed in a tungsten boat. On the surface of the sample, a 0.73 mm-diameter-hole shadow mask was placed to define electrode dots. The chamber was vacuum-pumped until to reach the vacuum level of $1x10^{-5}$ Torr or below. As applied with high current (150 ~ 200 A) through the tungsten boat, the boat and the source material inside the boat was heated above the melting point of the metal source. Then, the metal layer was deposited with the rate of 3~4 Å/sec. Usually, the deposited metal layer was 15 nm thick. The entire process is illustrated in Figure 2.3.

For smaller size electrodes (0.35 mm squares: the sample for Figure 2.4), photolithography and a liftoff process were employed. By photolithography, the square shaped electrodes were defined on a photoresist layer. First, photoresist (Microchem, S1805) was spin-coated on a sample with 3000 rpm speed for 30 sec to acquire a 500 nm-thick photoresist layer. A photomask was aligned on a wafer with a mask-aligner (Karl Suss, MJB-3) prior to the exposure. The mask-aligned sample was exposed to Hg_2 UV light. After development with a photoresist developer (Microchem, 351), a 15-nm thick plain Ag layer was deposited on the sample. When the photoresist layer was removed with acetone, the Ag layer on photoresist was lifted off, and the Ag layer on SiO_2 was left intact.

In order to enhance the endurance/connectivity of gate electrode over repeated pulse drives, for some samples cases (e.g., the sample in Figure 5.4), a 10-nm-thick Pt layer (Kurt J. Lesker, 4N purity) was sputter deposited on top of the Ag electrodes using the same shadow mask. For other purpose, a Si_3N_4 layer (e.g. the sample in Figure 5.7) was also sputter deposited on a sample. To start with, a source material (sputter target) was mounted on a RF magnetron gun, and a sample was positioned 2 inches above the source, aligned with the source. The chamber was vacuum-pumped to the level of $1x10^{-5}$ Torr or below. Ar_2 gas was then introduced to the chamber to the pressure level of $5x10^{-3}$ Torr. A RF magnetron gun was supplied initially with 30 W RF power in order to ignite Ar plasma. Eventually the RF power was lowered to 10 ~ 15 W for deposition. The specific conditions for Pt and Si_3N_4 deposition are listed in Table 1 and 2, respectively.

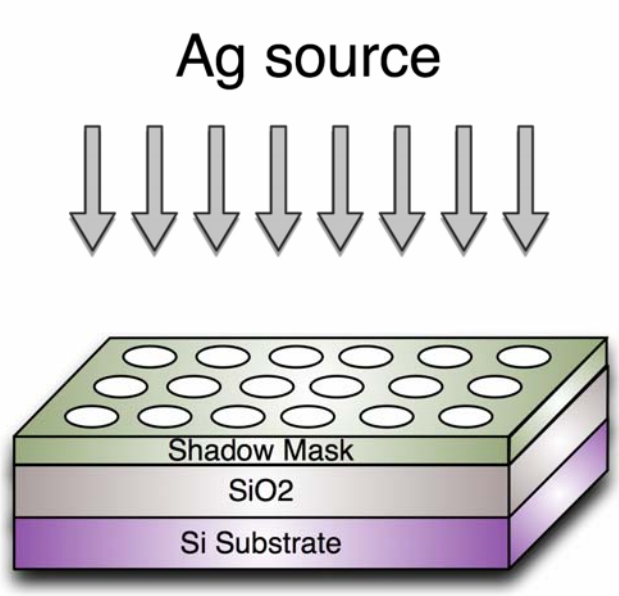

Figure 2.3 Circular electrode deposition with 0.73-mm-diameter-hole shadow mask by Ag evaporation

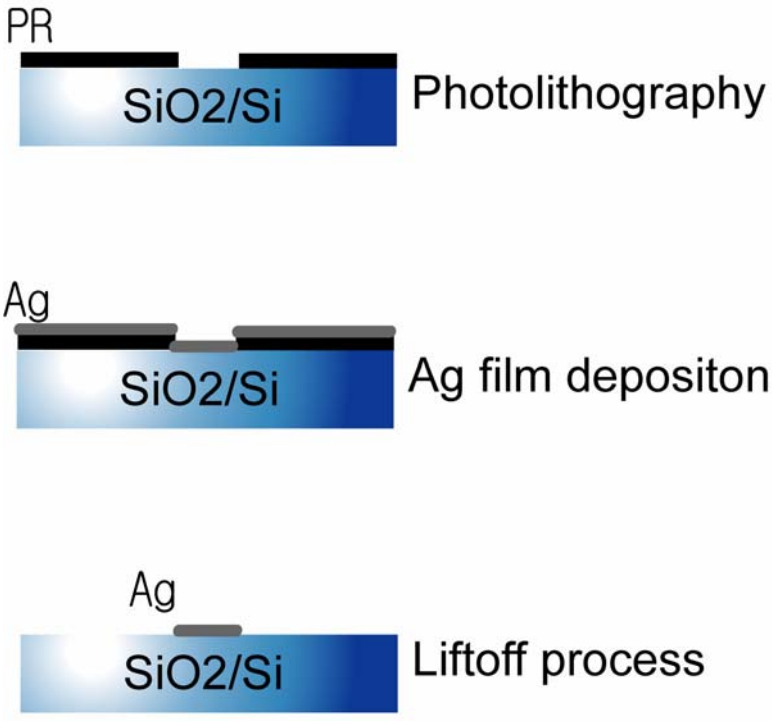

Figure 2.4 Lift-off process for 0.35 mm x 0.35 mm square Ag electrode deposition

Table 2.1 RF magnetron sputtering condition for Pt layer deposition

Target	Pt
Gas	Ar
Base vacuum pressure	$1x10^{-5}$ Torr
Gas pressure	$5x10^{-3}$ Torr
Power	10 W
Temperature	Room temp.
Deposition rate	55 Å/min

Table 2.2 RF magnetron sputtering condition for Si_3N_4 layer deposition

Target	Si_3N_4
Gas	Ar
Base vacuum pressure	$1x10^{-5}$ Torr
Gas pressure	$5x10^{-3}$ Torr
Power	15 W
Temperature	Room temp.
Deposition rate	11 Å/min

3.0 CURRENT TRANSPORT MECHANISM IN A MOS STRUCTURE

In an ideal MOS device, the current flow through oxide should be zero. However, at sufficiently high electric field or high temperature, carriers of an actual MOS device start to flow as part of an oxide breakdown process. The carrier transport characteristic is dependent on oxide thickness, and the electric field applied to the MOS structure. In general, four different types of carrier transport mechanisms have been reported, that can describe the current flow through an oxide layer; Fowler-Nordheim, Poole-Frankel, ballistic transport, and space-charge-limited transport. In this research, the oxide thickness is designated to be thin ($\leq$ 10 nm), and the electric field inside the oxide is very strong (~10^8 V/cm). Understanding the current transport mechanisms across the thin oxide under high field strength is one of the objectives of this study.

The energy band diagram of the MOS structure in the inversion regime operation (i.e. with a positive voltage pulse applied to the gate) is shown in Figure 3.2. Electrons from the Si substrate are injected into the oxide initially via a Fowler-Nordheim tunneling process. The injected electrons are accelerated under the high electric field and impact-ionize the gate metal, inducing Coulomb explosion[36,38,39,40]. As a result of the explosive fragmentation of electrode metal, strong atomic luminescence is observed. In this chapter, we will discuss the mechanisms of current flow and oxide breakdown process.

3.1 EVOLUTION OF I-V CHARACTERISTIC OVER REPEATED PULSE DRIVE

3.1.1 Experimental Setup

The *I-V* characteristic was measured after each electrical pulse. The experiment was designed to investigate the evolution of leakage current during oxide breakdown process at the application of voltage pulses of either positive or negative polarity. Application of high voltage pulses is expected to lower the interfacial potential barrier, increasing the leakage current. Pulses (+100 V amplitude and 10 ms width) were repeatedly applied to the MOS structure. After each pulse, the *I-V* characteristic was measured for $0 < V < 10$ V. HP 214B was used as a high voltage pulse generator ((+)/(-)100 V amplitude and 10 ms width). HP 4145B was used as an *I-V* characterization machine. During each application of pulses and I-V measurement, luminescence was measured with a spectrometer in UV (B&W Tek, BRC-111A-UV) and VIS-NIR (B&W Tek, BRC-111A-VIS/NIR) range. The sample tested in this experiment has a structure of 10-nm Pt/15-nm Ag/8-nm SiO_2/p-type Si.

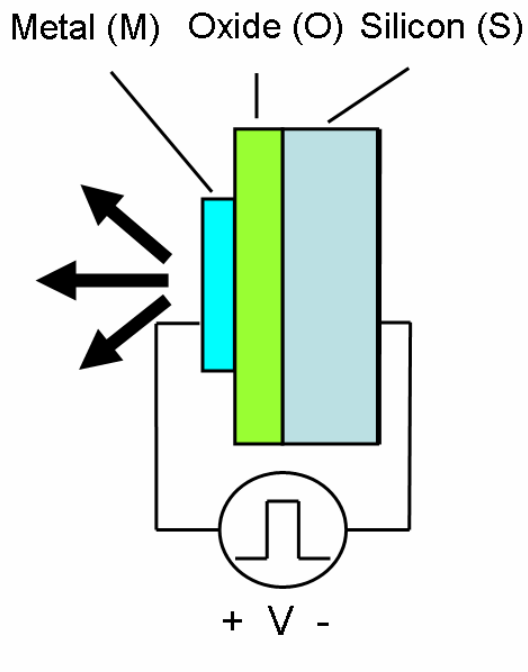

Figure 3.1 Structural diagram of experimental sample and test setup

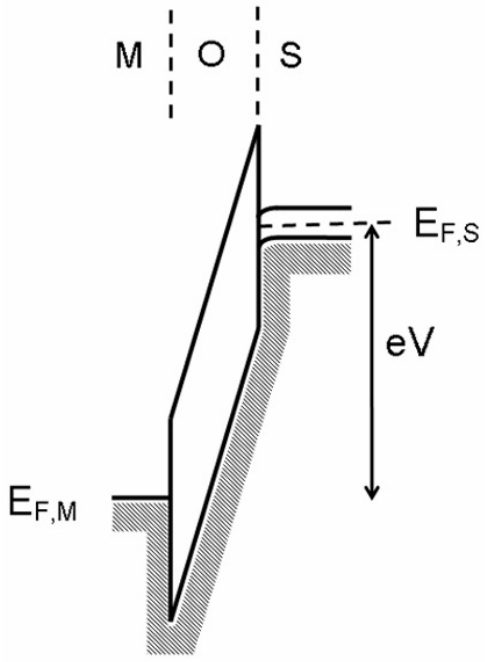

Figure 3.2 Band diagram of the MOS structure under application of positive voltage at the gate

3.1.2 Results

After application of initial 4~5 pulses, a burst of emission was first observed. The spectrum of emission (Figure 3.3) clearly reveals that the burst of emission came from atomic luminescence. The atomic elements observed from the spectroscopy are Ag, Si, Pt, and O. These elements are the main components of the gate and dielectric of the MOS structure. Details about atomic emission will be discussed at Chapter 6. The initial 4~5 pulses, which did not produce luminescence, correspond to the pre-breakdown step[45], during which the leakage current increases to the level required for Coulomb explosion.

Figure 3.4 clearly shows how *I-V* characteristic of the MOS structure evolves over repeated application of a pulse (+100 V amplitude and 10 ms width): For a fresh sample (before pulse drive), current density stayed at ~10^{-8} A/cm^2 due to tunneling-limited current effect, read at $V < 6$ V. A significant increase of current density, up to the 10^{-3} A/cm^2 level, was observed after the first pulse, and then to the 10^{-2} A/cm^2 level after the second pulse, all read at 10 V. After the fifth pulse, it settles at around the 10^{-1} A/cm^2 level. For the case of application of a negative pulse (-100 V and 10 ms width), *I-V* characteristic is measured after each pulses, (Figure 3.5). Similarly, for a fresh sample (before pulse drive), current density was measured as ~10^{-7} A/cm^2, read at $V<4V$. This is approximately one order higher than the positive pulse case. After the first pulse, current density jumps up to 10^{-1} A/cm^2 level, read at 10 V. Even at additional application of pulse, current density stays at 10^{-1} A/cm^2 level, read at 10 V. This imposes that major oxide break down occurs during the first pulse, which is reasonable in the sense that the majority carrier can easily induce a high current flow.

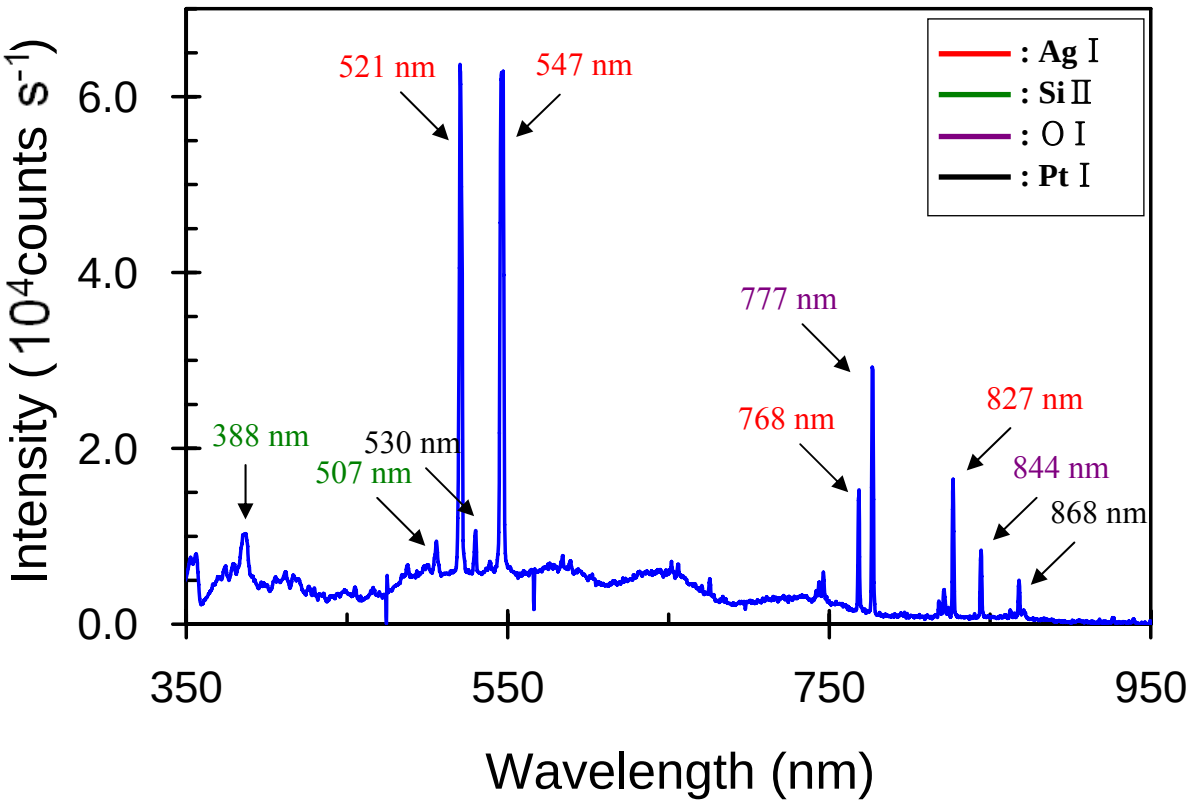

Figure 3.3 VIS range electroluminescence of a 10 nm Pt/15 nm Ag/8 nm SiO_2/p-type Si structure at application of pulses with +100 V gate voltage and 10 ms pulse width

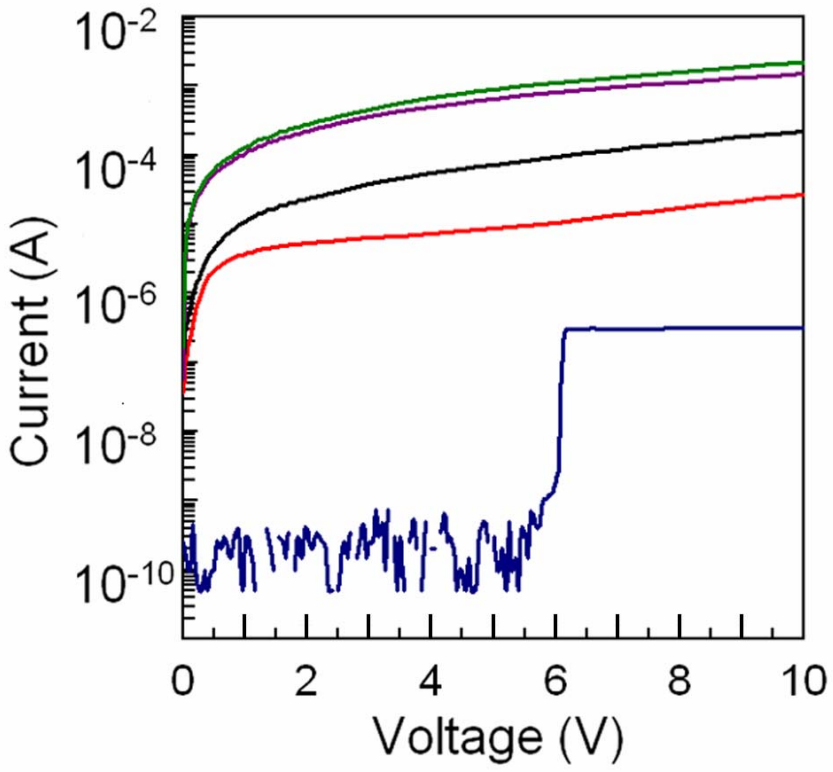

Figure 3.4 The *I-V* curves of a sample (10-nm Pt / 15-nm Ag / 8-nm SiO_2 / p-Si) measured before and after pulsed drive (100 V, 10 ms): fresh sample (blue); after the first drive (red); after the second pulse (black); after the fifth pulse (purple); after the twentieth pulse (green)

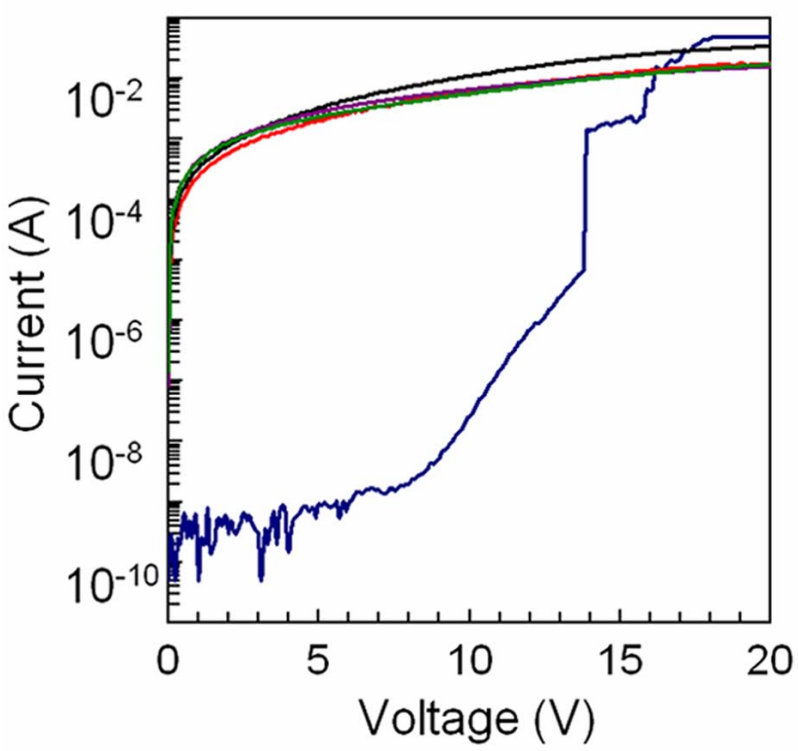

Figure 3.5 The *I-V* curves of a sample (10-nm Pt / 15-nm Ag / 8-nm SiO_2 / p-Si) measured before and after pulsed drive (-100 V, 10 ms): fresh sample (blue); after the first drive (red); after the second pulse (black); after the fifth pulse (purple); after the twentieth pulse (green).

3.2 CURRENT FLOW THROUGH LEAKAGE CHANNELS FORMED IN A MOS STRUCTURE

3.2.1 Experimental Setup

The *I-V* characteristic was measured in a broader range (0~100V) in an effort to develop a better understanding of carrier transport phenomenon during the pulse drive that produced atomic luminescence. With the same setup as above, we applied 0 ~ 100 V voltage sweep. We also made smaller dimension of electrode dots (0.35 mm x 0.35 mm square with 15 nm thickness, Ag) in order to stay within the instrument current limit (20 mA at 100 V). For the smaller size electrodes, photolithography and a liftoff process were employed. With this small electrode, current reached 19 mA maximum at 100V.

3.2.2 Results

The *I-V* characteristic of a Si MOS was measured at $0 < V < 100$ V and is plotted in the log-log scale (Figure 3.6). The *I-V* curve shows an Ohmic behavior in the low voltage range ($V < 3V$). For $V > 3$ V, the slope gradually increases to 1.5. The $V^{3/2}$ voltage-dependence is characteristic of the Child-Langmuir space-charge-limited current in a narrow gap with parallel electrodes:

$$J = \frac{4}{9}\varepsilon\sqrt{\frac{2e}{m^*}}\frac{V^{3/2}}{d^2} \quad \text{.....(2)}$$

where ε is the permittivity of gap insulator, m^* is the effective mass of electron, and d is the gap size. Assuming the free-space permittivity for ε and a free-space electron mass for m^*, the formula produces an injection current of ~10^9 A/cm^2 at V = 100 V and d = 10 nm. This closely matches the channel current density estimated at chapter 3.1.2 based on the *I*-*V* measurement result. This Ohmic-to-space-charge-limited transition indicates that injected carrier density becomes dominant over the volume generated carrier density. This space-charge-limited current formula assumes ballistic transport of electrons across the gap with negligible barrier height for carrier injection [28,46].

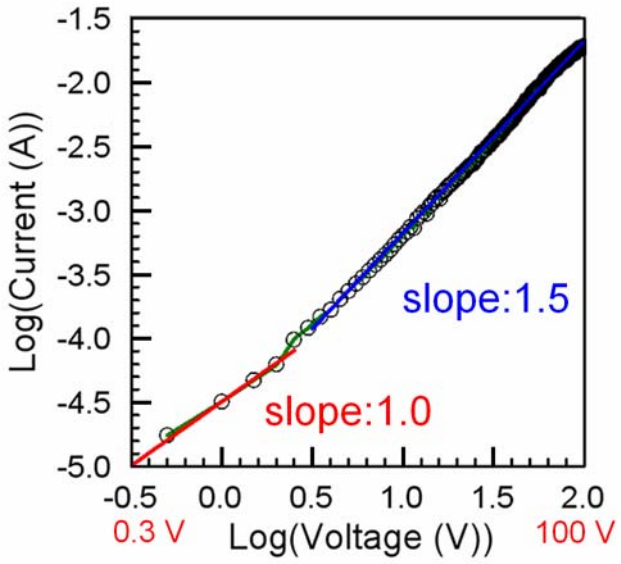

Figure 3.6 The log-log scale plot of the *I-V* curve of a sample (15-nm Ag / 8-nm SiO_2 / p-Si) after ten pulsed drives. Above 3 V, the slope increases to 1.5, which indicates a space-charge-limited current transport

3.3 DISCUSSION

This work provides a good understanding of how an oxide layer breaks down and the mechanism of current flow across the oxide layer. It should be noted that after the initial oxide breakdown, the Child-Langmuir space-charge-limited current mechanism plays a critical role in the Coulomb explosion. The observation of $V^{1.5}$-dependence of current is a strong evidence of highly kinetic electrons. With the initial breakdown process, the barrier height for electron injection at the SiO_2/Si interface is believed to be significantly reduced, and this allows for injection/transport of a large number of kinetic electrons through leakage channels [23,24,31,32].

4.0 ELECTRICALLY INDUCED COULOMB EXPLOSION

As discussed in Chapter 1, Coulomb explosion has been observed only with high-intensity (10^{14} W/cm^2) short (<10 ps) lasers so far. Now, in this thesis, we observed electrically induced Coulomb explosion for the first time. Injection of kinetic electrons into metal/SiO_2 interface was discussed in the previous chapter. Observation of highly kinetic electrons is one of the core requirements for electrically induced Coulomb explosion. Injected, highly kinetic electrons are believed to collide with metal atoms at the interface between metal electrode and oxide. In metal, ionized metal atoms are known to be rapidly quenched by thermal electrons. Due to this reason, it has been known to be very hard to keep the ionized metal atoms in bulk. When ionization process is significantly faster than thermalization, metal ions can accumulate and electric charge will increase in the local area. When the Coulombic repulsion energy is greater than the binding energy of metal atoms, sudden explosion will occur.

The fragmented metal atoms will take different relaxation paths, depending on their charge states (neutral or ion). In the case of neutrals, the excited Ag atoms will take an internal relaxation process with possible emission of photons. In the case of atomic ions, the Ag atoms will go through a recombination process with electrons. This ion-electron recombination process is expected to occur either in a radiative recombination or in another process called dielectronic recombination [33,34]. The former is the inverse photoionization process and is known to be efficient with relatively low energy of electrons. The latter is a resonant one, in which an

incoming electron excites an electron of the ion for the amount of energy gained by capturing the incident electron. The state in which the incident and second electrons are both in excited orbitals of neutral Ag atom is not stable, and can undergo a transition to a stable state of the neutral atom, emitting photons. This dielectronic recombination is the phenomenon commonly observed in high-temperature plasmas, upper atmosphere, and distant stars [33,34].

Before we introduce our observation of electrically induced Coulomb explosion, requirements for the Coulomb explosion should be discussed. For a material system with the electron impact ionization cross section, σ and the relaxation (deionization) time, τ, the threshold level of kinetic electron injection required for Coulomb explosion can be expressed as $J = e/\sigma\tau$, where e is the electron charge. The nonequilibrium distribution of femto-second laser-heated electrons in metal is known to be thermalized in the time scale of ~1 ps via electron-electron scattering and electron-phonon coupling [35]. In the case of electrical excitation like the present work, some of the injected electrons in the metal layer will escape away, since unlike the laser excited case the probe-contact region has no surface potential barrier to confine the electrons. The relatively poor confinement of injected electrons in the present work suggests longer lifetime of ions compared to the optical excitation case. Assuming $\sigma = 5\text{x}10^{-16}$ cm^2[37], and $\tau \geq 1$ ps, the upper bound of threshold injection level for Coulomb explosion is estimated to be $2\text{x}10^{27}$ cm^{-2}-s^{-1}, or $3\text{x}10^8$ A/cm^2 in terms of current density.

In the present work, we report electrically induced Coulomb explosion, which requires highly kinetic electron impact-ionization of metal atoms. Following evidences strongly support our explanation; generation of highly kinetic electron by electric field acceleration through nano-channel in oxide layer, atomic luminescence, deformation pattern, current density above the required level for Coulomb explosion, and *I-V* measurement.

4.1 SUPPORTING MEASUREMENT DATA

4.1.1 Atomic luminescence

For the experiment, we prepared a standard Si MOS structure according to the steps discussed in Chapter 3. The gate electrode is supplied with positive voltage, and the substrate is connected to the ground. Pulse generator (HP 214B) applies 100 V pulses with 10 μs width. A multimode optical fiber of core diameter 1 mm is placed in close proximity to the electrode (1~2 mm gap) in order to collect luminescence during electrical pulse drive. The light coupled into the fiber is sent to a CCD-based optical spectrum analyzer. The overall setup is shown in the Figure 4.1.

Figure 4.2(a) shows luminescence spectrum in the UV range (200 nm~400 nm) and Figure 4.2(b) shows spectrum in the VIS/NIR range (400 nm~1050 nm). 328 nm, 338 nm, 521 nm, 547 nm, 768 nm, 827 nm lines are atomic luminescence of neutral Ag. Silicon and oxygen lines are also observed.

It is also interesting to note in Figure 4.2 that the luminescence originating from Si^{2+} ions (e.g., the 590 nm line) is clearly observed whereas none from Ag^{2+} ions [10,11]. The impact ionization energies of Ag, Ag^{+}, Si, and Si^{+} are 7.5 eV, 21 eV, 8.2 eV, and 16 eV, respectively [37]. It is then inferred that the kinetic energy of injected electrons involved in the present work ranges up to over 16 eV. In the case of moderately-high field strength (10^7 V/cm) in 5-to-10-nm-thick SiO_2, the tail of energy distribution of electrons in the oxide is known to extend up to 7-8 eV [41,42]. In the case of defect channels formed in oxide, the ballistic nature of electron

transport seems to be significantly enhanced, enabling the attainment of high kinetic energy (up to ~16 eV) under the strong electric field (~10^8 V/cm).

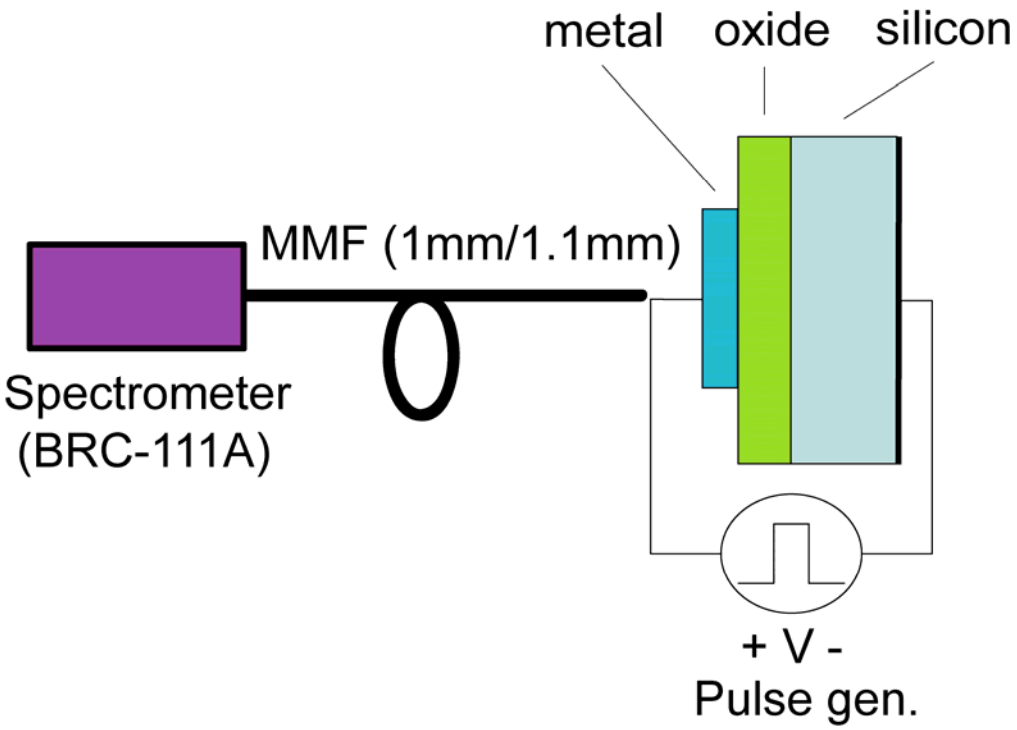

Figure 4.1 Diagram of spectrum measurement setup for the MOS structure

(a) (b)

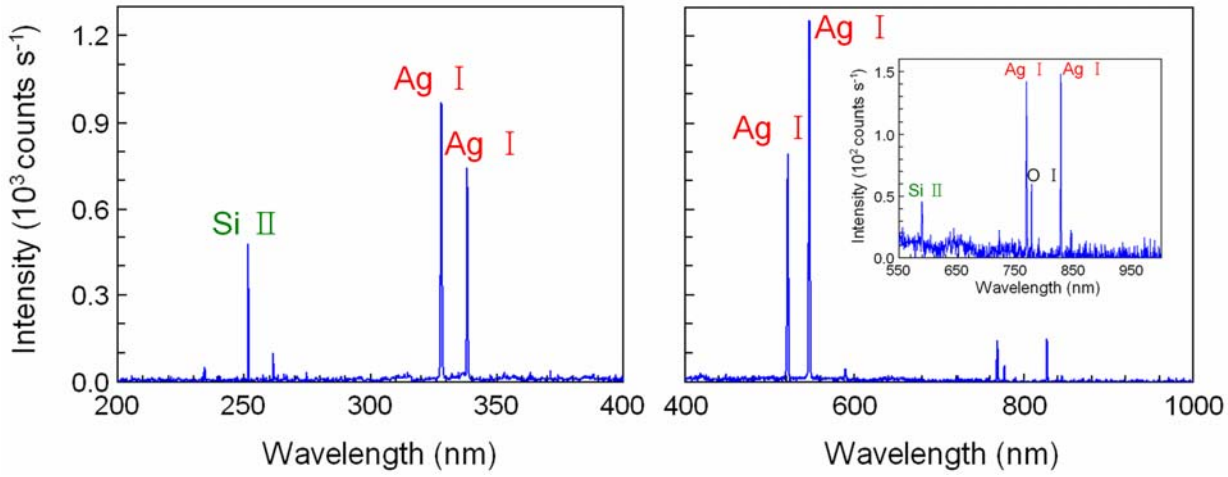

Figure 4.2 Luminescence spectra from a Si MOS structure (15-nm-thick Ag / 8-nm-thick SiO_2 / p-type Si substrate) under positive voltage pulses (100 V amplitude; 10 ms width) applied to the gate, (a) in UV range(200-400 nm), and (b) in VIS/NIR range (400-1000 nm). The inset is the 10x magnification of the intensity for the spectral range of 550-900 nm

4.1.2 Current density

Figures 3.4 & 3.5 in Chapter 3 show how *I-V* characteristic of the MOS structure evolves over repeated application of a pulse (±100 V amplitude and 10 ms width). For a fresh sample (before pulse drive), current density stayed at ~10^{-8} A/cm^2, read at $V < 6$ V, showing a tunneling-limited current effect. Significant current density increase was observed up to the 10^{-3} A/cm^2 level after the first pulse, and then to the 10^{-2} A/cm^2 level after the second pulse, all read at 10 V. After the fifth pulse, it settles at around the 10^{-1} A/cm^2 level. This dramatic increase of current is attributed to formation of localized leakage paths in the oxide and induces atomic luminescence as discussed above. Assuming approximately 3-nm-diameter leakage channels [23,43,44] with an areal density of 4×10^6 cm^{-2} (i.e., 5 μm average spacing), the measured injection current (0.5 A at 100 V: Figure 4.3) translates into a current density of ~5×10^8 A/cm^2 in the individual nano-channels. This number is sufficiently greater than the upper bound of injection threshold estimated above as a requirement for Coulomb explosion. Overall this *I-V* analysis supports that the requirements of Coulomb explosion, i.e., injection of kinetic electrons with high current density, can be met in the MOS structure with the nanoscale channels formed in oxide.

4.1.3 Temporal profiles of L-I-V characteristic during pulse drive

The hypothesis being tested in this chapter is whether electron impact ionization can produce/accumulate ions fast enough such that they can reach an explosion threshold before thermalization. In order to elucidate the underlying mechanisms of kinetic electron injection, impact ionization, and atomization processes, we have characterized the time dependence of injection current and luminescence intensity under a pulsed voltage drive. Single voltage pulses (+100 V amplitude and 10 ms pulse duration) were repeatedly applied to the gate with an interval > 60 s, and the current and luminescence transients were recorded during each drive.

Figure 4.3(a) shows the first luminescence transient observed during the fifth pulse: the measured luminescence intensity corresponds to the integral power captured over the visible-to-NIR range of spectrum of Ag atomic luminescence. For the first 2.5 ms duration, no luminescence was detected, and then a burst of emission suddenly appeared, which lasted for ~100 μs. (No luminescence was observed during the first four pulses, although the injection current remained at a nearly constant level at ~1 A for the entire pulse duration.) The charge injection time counted up until the on-set of luminescence is ~40 ms. From the injection level (800 mA) and duration (40 ms), the total amount of charges injected into the oxide is estimated to be 0.032 C, or 8 C/cm^2 when normalized with the electrode area (3.9×10^{-3} cm^2). This well matches the charge-to-breakdown values reported in literature for a Si MOS structure with similar oxide thickness (1-100 C/cm^2 at 10 nm) [31,32]. This transient measurement result clearly suggests that the burst of emission occurred with oxide breakdown. A large amount of kinetic electrons injected through the oxide are then believed to have caused atomization of Ag and thus atomic luminescence. From the sixth pulse or after, luminescence occurred in

synchronization with the rising edge of the voltage/current pulse, and this indicates that once an initial breakdown occurs, kinetic electrons can be readily injected (Figure 4.3(b)). A close look at the transient profile reveals numerous, persistently occurring current spikes during the luminescence. Also many fine features are observed in the luminescence transient, although overall the luminescence intensity monotonically decays (Figure 4.3(c)). This suggests occurrence of a multitude of small localized explosions during the luminescence period (~100 μs), instead of a single global explosion. These 'mini-explosions' might be associated with the microscopic structures intrinsic to the metal electrode, i.e., granular structures of a Ag layer. The spatial extension of the individual mini-explosions may be on the same scale with the grain/crystallite sizes (~10 nm) of the film. This estimate is consistent with the discussion made above with the image of Ag atomic luminescence (Figure 5.2). This further suggests involvement of nanoscale, localized leakage channels in oxide, through which kinetic electrons are injected impact-ionizing individual metal nanostructures [23].

In the case of a MOS formed on an n-type Si (with a +100 V, 10 ms pulse applied to the gate), a drastic difference is observed (Figure 4.4(a)). The luminescence lasted only for ~1 μs, about two orders of magnitude shorter than the p-type substrate case. Electrons abundantly introduced to the gate/oxide interface are expected to readily neutralize the metal ions that are being formed via impact ionization. This would reduce the lifetimes of metal ions, and therefore the chance to get into a Coulomb explosion. When +50 V, 10 ms pulse applied instead of +100 V, interestingly while luminescence intensity stays at the same level, luminescence lasted for a significantly longer time (~50 μs) in Figure 4.4(b). Increase of luminescence time at lower voltage indicates that luminescence is dependent on the amount of injected current.

(a) (b)

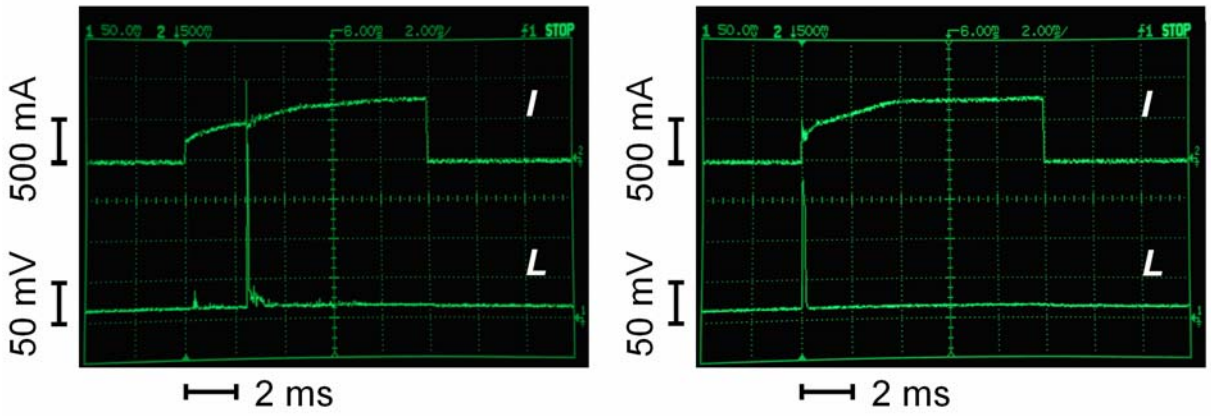

(c)

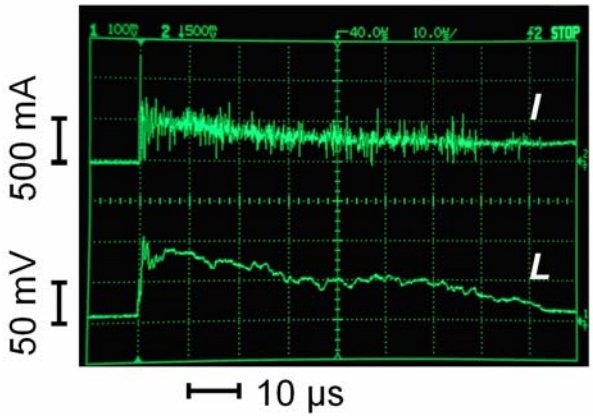

Figure 4.3 A MOS structure formed on a p-type Si substrate (10-nm Pt / 15-nm Ag / 8-nm SiO_2 / p-Si) (**a,b,c**). Current (*I*: top trace) and luminescence (*L*: bottom trace) profiles during the fifth drive (**a**) and during the sixth drive (**b**). A magnified view of the transients during Coulomb explosion (the seventh drive) (**c**).

(a) (b)

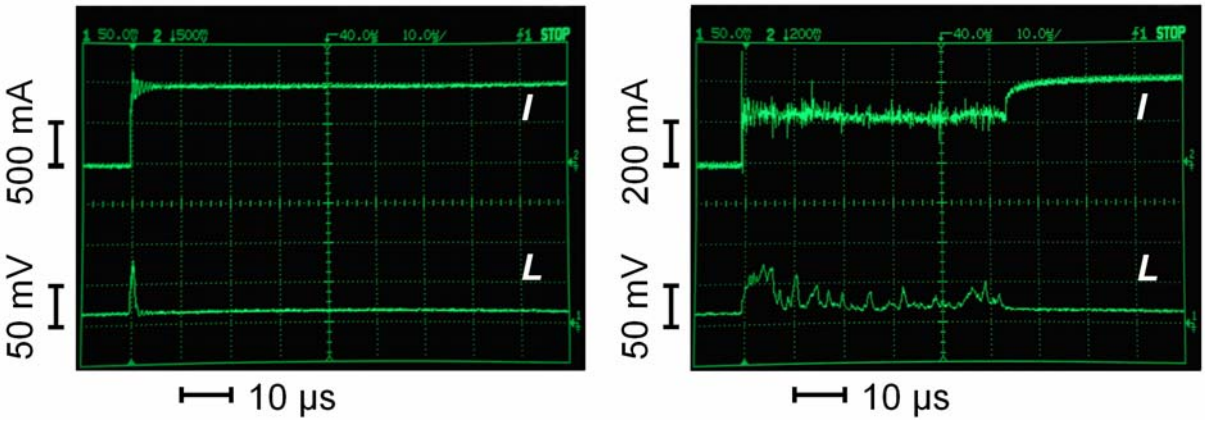

Figure 4.4 (10-nm Pt / 15-nm Ag / 8-nm SiO_2 / n-Si) sample (a) *I-L* characteristic top+(with a +100 V, 10 ms pulse applied to the gate), (b) *I-L* characteristic top+(with a +50 V, 10 ms pulse applied to the gate)

4.1.4 Metal electrode deformation

The metal electrode layer appears to have deformed during explosion. In general, images of deformed area show two different deformation patterns. First pattern is a crater-like deformation. This crater-like pattern was observed, when pulses with short width (10 μs) were applied. This pattern appears to be a collection of small explosion centers (~3 μm length in diameter) of metal layer. From Figure 4.7, the deformed area also matches well with luminescence spots. The crater-like deformation is believed to be a result of Coulomb explosion. Another type of deformation is a ball-up pattern. This deformation usually is observed when pulse width is long (~10 ms). It should be noted here that the current flow remains at a constant level throughout the pulse duration (10 ms). This implies a continuous deposition of energy into the system. The temperature is then expected to rise monotonically during the pulse, which may lead to melting of the electrode metal. Optical microscopy inspection after each drive with various different pulse width reveals that the electrode surface morphology has evolved through at least two distinct stages, initially, crater-like microscale feature formation during the explosion, followed by major macroscale deformation that looks to be caused by melting during the post-explosion period of the pulse.

Figure 4.5 shows evolution of surface morphology of Ag electrodes over repeated application of electrical pulses (100 V amplitude and 10 μs width). The sample structure is 15-nm-thick Ag / 5-nm-thick SiO_2 / p-type Si. Ag electrode is a circular layer with 0.73 mm diameter. Figure 4.5(a) is an image of a fresh sample. Figure 4.5(b) is after the 3rd pulse drive. During the first two pulses there was no luminescence. During the third pulse, the first luminescence was observed. The Ag metal in the region around the probe-touched area (left-

hand side) is found to have erupted with microscale extension. Figure 4.5(c) is a close-up view of the eruption pattern. The erupted area shows a random, but connected network pattern. The erupted area extends about 3 μm in the lateral dimension. The average spacing between eruption centers is estimated to be ~ 5 μm. Figure 4.5(d) is after the 4^{th} pulse drive (i.e., after the second luminescence burst). Eruption with a pattern similar to the first one Figure 4.5(c) is found added, and overall the eruption area increased. Figure 4.5(e) is after the 15^{th} pulse. More eruptions occurred, resulting in a dense, uniform network over the entire electrode surface. The fragmented Ag atoms appear to have precipitated into nano/micro particles after explosion, as can be seen as small dots scattered across the electrode. It was observed that the luminescence occurs from near the stylus area to the outer edge area. After deformation, conductivity of deformed area drops rapidly. In other words, after explosion, current density through nano-channel will be minimal, while nano-channels at other area are formed and inject current to the electrode.

On the other hand, Figure 4.6 shows evolution of surface morphology of Ag electrodes over repeated application of electrical pulses (100 V amplitude and 10 ms width). The sample structure is 15- nm-thick Ag / 10-nm-thick SiO_2 / p-type Si. In this case, the Ag electrode is 0.35 mm x 0.35 mm square. Figure 4.6(a) is fresh sample. Figure 4.6(b) is after the 5^{th} pulse drive (i.e., after the first luminescence). During the first four pulses there was no luminescence. The electrode shows a global deformation after the 5^{th} pulse. The probe-touched area is seen in the right hand side. Figure 4.6(c) is a close-up view of the deformed surface. Ag metal balled up forming microscale islands.

Figure 4.7 is images of atomic luminescence during explosive fragmentation of Ag electrode of a Si MOS structure and the resulting surface morphology of the electrode. Sample structure was 15-nm-thick Ag / 10-nm-thick SiO_2 / p-type Si. Ag electrode is 0.73-mm-diameter

circular layers. Figure 4.7(a) shows surface morphology of Ag electrode after the first explosive fragmentation (i.e., after the first luminescence burst) during a pulsed drive (100 V amplitude, 100 μs width). Figure 4.7(b) is a luminescence image captured by a CCD camera during the explosion. The green luminescence is observed across the electrode area with higher intensity around the probe (bottom center). In Figure 4.7 (c), the luminescence image Figure 4.7(b) was superposed on the electrode morphology image Figure 4.7(a). The distribution of luminescence centers (green dots) strongly correlate with the electrode deformation pattern (microscale eruption of Ag metal around explosion sites: see Figure 4.5for a close-up view of the eruption area): green dots are more densely populated along and around the eruption area.

When 10 ms pulses are applied, luminescence burst occurred only once and the electrode was fully deformed after the first luminescence, forming the morphology like Figure 4.6. Each electrode dot was only for one time use. By measuring sheet resistance of electrode, we figured out the electrode conductivity drops dramatically after the first luminescence. Resistivity of the deformed electrode was $1M\Omega \cdot cm^2$. To see the effect of electrode connectivity, we deposited additional 10 nm Pt exactly overlapped on worn-out electrode dots. This experiment suggests that only if the electrode conductance is sufficiently high, we can generate atomic luminescence for longer period of operation. We chose Pt instead of any other material as an additional conductive layer, because Pt is known as the most stable metal, difficult to ionize, consequently not easily fragmentized. With the help of an additional Pt layer, luminescence life time at +100 V and 10 ms pulse increased by 20~30 times, compared with the 15 nm-Ag only electrode layer sample case. Accordingly, intensities of Ag atomic luminescence in the spectrum increased. Figure 5.5 shows enhancement of intensity by the additional Pt layer.

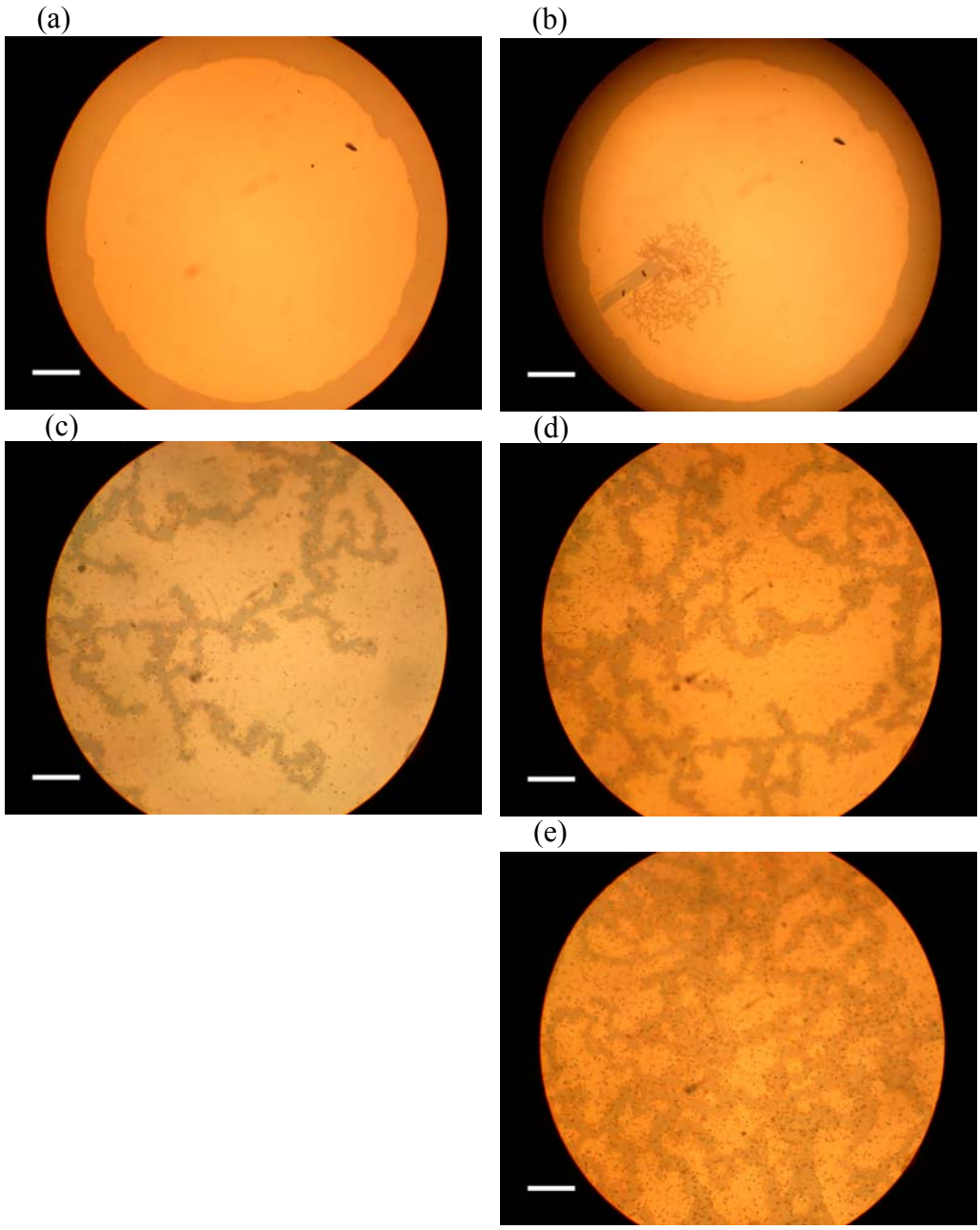

Figure 4.5 Evolution of surface morphology of Ag electrodes over repeated application of electrical pulses (100 V amplitude and 10 μs width).: Sample structure: 15-nm-thick Ag / 5-nm-thick SiO_2 / p-type Si. Ag electrode: 0.73 mm diameter. (a) fresh sample (scale bar, 100 μm). (b) after the 3rd pulse drive. (first luminescence) (c) A close-up view of the eruption pattern. (scale bar, 10 μm). (d) after the 4th pulse drive (i.e., after the second luminescence burst). (e) after the 15th pulse.

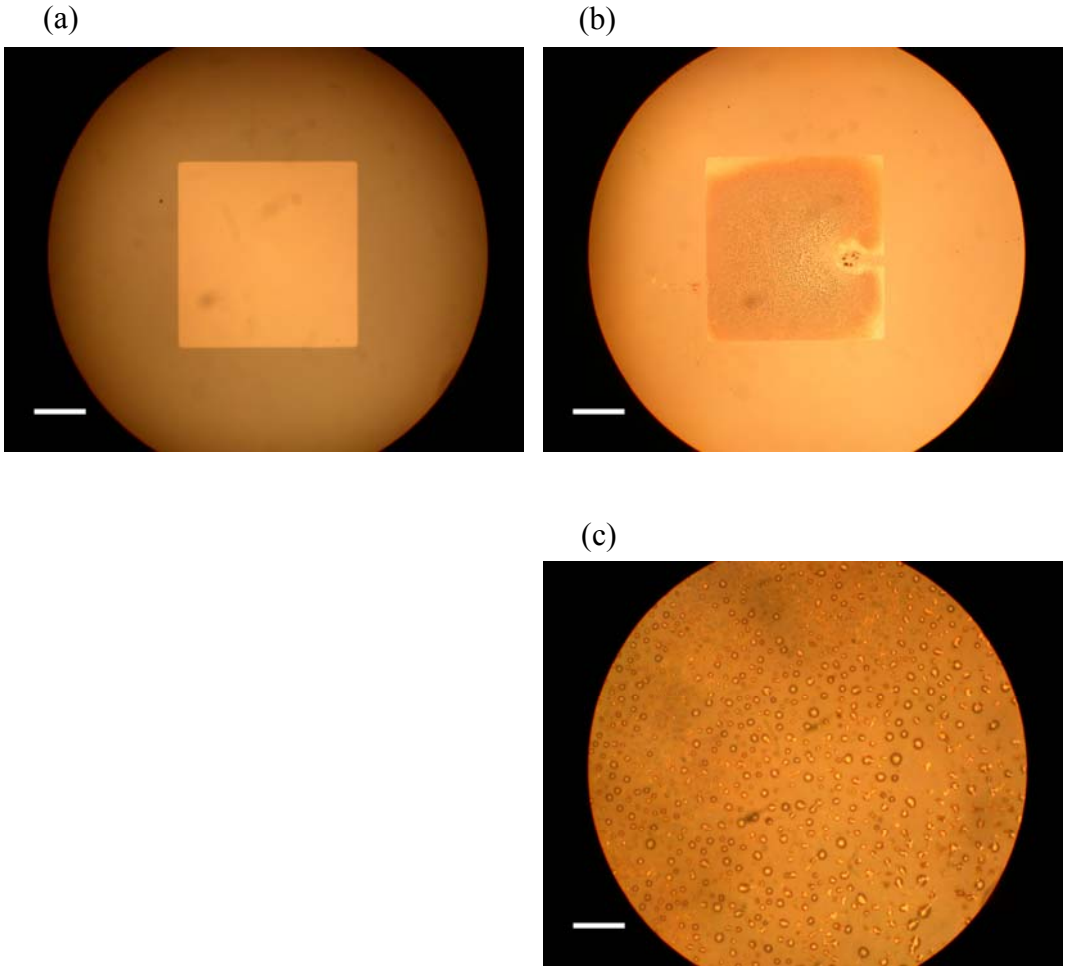

Figure 4.6 Evolution of surface morphology of Ag electrodes over repeated application of electrical pulses (100 V amplitude and 10 ms width).: Sample structure: 15- nm-thick Ag / 10-nm-thick SiO_2 / p-type Si. Ag electrode: 0.35 mm x 0.35 mm square. (**a**) fresh sample (scale bar, 100 μm). (**b**) after the 5^{th} pulse drive (i.e., after the first luminescence). (**c**) A close-up view of the deformed surface. Note the scale change (scale bar, 10 μm).

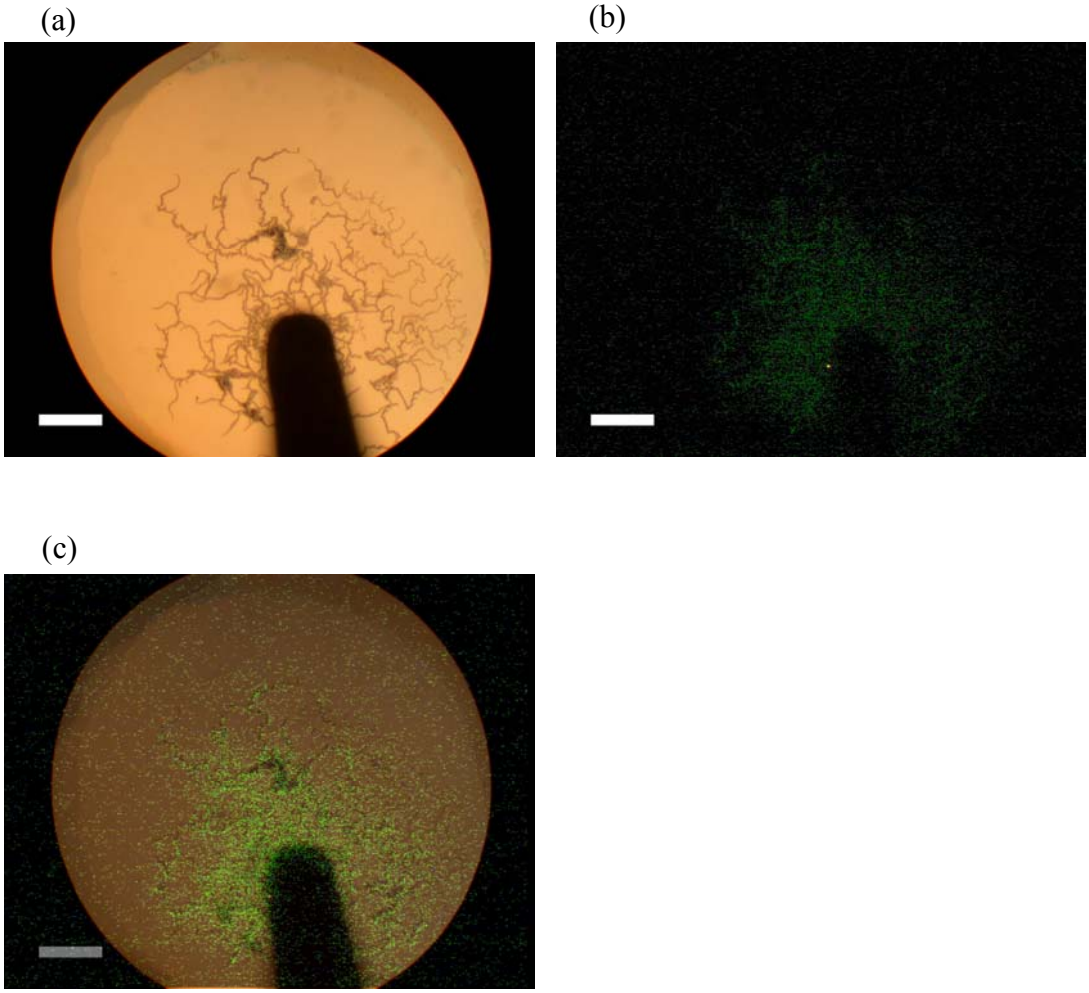

Figure 4.7 Images of atomic luminescence during explosive fragmentation of Ag electrode of a Si MOS structure and the resulting surface morphology of the electrode. (a) Surface morphology of Ag electrode after the first explosive fragmentation (i.e., after the first luminescence burst) during a pulsed drive (100 V amplitude, 100 μs width) (scale bar, 100 μm). (b) Luminescence image captured by a CCD camera during the explosion. (c) The luminescence image (b) superposed on the electrode morphology image (a).

4.2 DISCUSSION

Coulomb explosion has been mainly reported in experiments performed with ultra-short, high intensity laser pulses [3-6]. In this thesis, we observed the Coulomb explosion induced by electrons. We discussed the requirement for Coulomb explosion. First, current injection level should be higher than the threshold level, which is calculated to be $3x10^8$ A/cm^2 in current density. The measured current density was $5x10^8$ A/cm^2, which is similar or higher than the threshold level. Second, the energy distribution of electrons should reach a certain range, sufficiently high for ionization of metal atoms. The injected electrons are believed to be accelerated by strong electric field and collide with metal atoms at the interface between metal electrode and oxide. As a result of coulomb explosion, atomic luminescence was observed, which will be discussed in next chapter.

5.0 ATOMIC LUMINESCENCE IN A MOS STRUCTURE

Optical atomic spectroscopy includes atomic emission, absorption and luminescence spectroscopy. These involve valence electron transitions, which usually correspond to the radiation wavelengths in the UV to visible or IR range. Absorption or emission spectra are measured from isolated atoms at ground (or near-ground) levels or at excited states, produced by thermal evaporation, arc discharge, or a plasma process. Methods of atomization/excitation can be categorized into thermal (flames and electrothermal), electrical (cathodic arc/glow discharges and other types of plasma discharge) or optical (laser-induced breakdown).

A commonly employed method for elemental analysis is the inductively-coupled-plasma atomic emission spectrometry (ICP-AES). Despite its wide applicability, the conventional ICP is anchored to a laboratory instrument. This is mainly due to the size, weight and gas consumption involved with the ICP operation.

In the previous chapters, we reported the strong atomic luminescence as a result of Coulomb explosion. The observation of atomic luminescence in our simple MOS structure is significant in that it can be applied for a simple element analysis. In this chapter, first, we will discuss the general aspect of the atomic luminescence. We will then discuss distribution and size of luminescence centers. Finally, the luminescence of other materials obtained from our simple MOS structure will be discussed.

5.1 ATOMIC SPECTRUM

Atomic luminescence was observed under a pulse drive with high voltage (50~100V) applied between front metal electrode (positive/negative voltage) and substrate. Pulse width was set in the range from 10 μs to 10 ms. On the top of front metal electrode, an optical fiber was used to collect luminescence light. The collected light was sent to the spectrometer (B&W Tek, BRC-111A) in UV or VIS/NIR range. The overall measurement setup is shown in Figure 4.1.

Figure 4.2 shows the atomic emission spectra resulting from the inversion regime operation of the MOS capacitor structure formed on a p-type Si substrate. The luminescence spectra were measured with +100 V pulses applied to the gate. All major lines in the figure correspond to the transitions of the neutral Ag atoms, and the minor lines are from the neutral and singly charged ion silicon and the neutral oxygen [9], Figure 4.2(a) shows the UV range (200-400 nm) and Figure 4.2(b) is for the visible to near-infrared (NIR) range (400-1000 nm). The UV range spectrum shows several atomic lines, with the 328 nm and 338 nm lines as major ones, and the 252 nm line as a minor one. These lines can be identified by the diagram of the energy level of Ag I [Figure 5.1]. The two major lines at 328 and 338 nm correspond to the 5p $^2P_{3/2}$ - 5s $^2S_{1/2}$ and 5p $^2P_{1/2}$ - 5s $^2S_{1/2}$ transitions of the neutral Ag atom, respectively. The 252 nm line is identified as an atomic line of Si II. The visible-to-NIR range spectrum reveals the 521 nm (5d $^2D_{3/2}$ – 5p $^2P_{1/2}$), 547 nm (5d $^2D_{5/2}$ – 5p $^2P_{3/2}$), 769 nm (6s $^2S_{1/2}$ – 5p $^2P_{1/2}$), and 827 nm (6s $^2S_{1/2}$ – 5p $^2P_{3/2}$) lines, all corresponding to the major transitions of the neutral Ag atom [9-11]. It is interesting to note here that these Ag atomic lines are persistent in this experiment. This

suggests that the Ag atoms excited during atomization relax in a cascade process following the energy level scheme, shown in Figure 5.1.

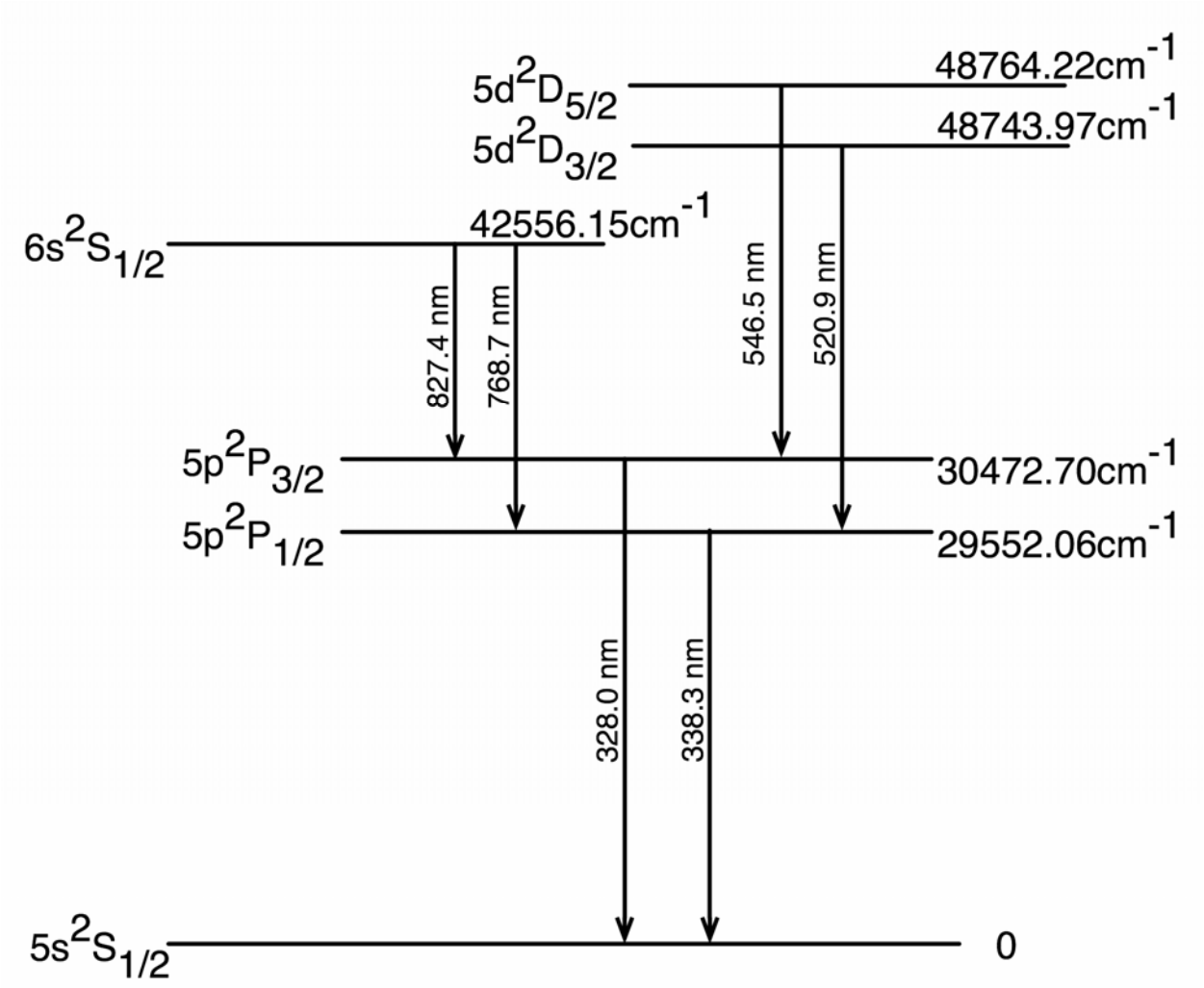

Figure 5.1 A schematic of electron transitions in the Ag neutral atom (Ag I)

5.2 ATOMIC LUMINESCENCE IMAGE

The Ag atomic luminescence from the MOS structure under pulsed excitation was imaged using a CCD camera (Nikon, Coolpix 995) in conjunction with an optical microscope (magnification: x250). The same excitation setup was used as for spectrum measurement. +100 V and 10 μs width pulse drive was applied to the gate of a MOS.

Figure 5.2 is a micrograph of atomic luminescence from a Ag gate electrode of a Si MOS structure under pulsed electrical excitation (accumulation of luminescence over 8 s with eight drives with a 60 V, 10 μs pulse with 1 s pulse interval). The overall color of emission is green, while less intense of purple light is also observed over all area. The green luminescence corresponds to the atomic lines in the visible range (521 nm and 547 nm), and the purple one is attributed to the UV lines at 328 nm and 338 nm.

After repeated occurrence of Coulomb explosion, the connectivity of the Ag electrode deteriorates, as confirmed by a sheet resistance measurement performed afterward. The finite conductance of the Ag electrode causes a potential drop across the electrode area itself. The actual amount of voltage applied across the gate oxide layer is then significantly lower in the region farther away from the probe point. A higher voltage across the gate oxide would result in higher kinetic energy of impinging electrons and a larger electron flux, thus providing a different ambient for excitation/relaxation of Ag atoms. The homogeneous nature of the Ag atomic luminescence indicates that Coulomb explosion occurred with a relatively uniform distribution across the electrode. A magnified view of the CCD image of the green luminescence, Figure 5.3, reveals that the luminescence centers (green or purple dots) are uniformly distributed at a

microscopic level with average distance of ~5 μm (i.e., with an areal density of ~$4x10^6$ cm^{-2}) (Figure 5.3). The size of individual luminescence centers is below the resolution limit of imaging (< 0.5 μm). This suggests involvement of highly localized, but uniformly distributed injection channels of kinetic electrons across the electrode area [23,24]. This is contrasting to the earlier reports on the breakdown behavior tested with Si MOS capacitors that have a much thicker oxide layer (20-100 nm thickness) [43]. In the thick oxide case, formation of major defects such as craters with 10-100 μm diameter has been reported.

As a further work of an additional Pt layer discussed in Chapter 4.1, the luminescence enhancement with a Pt layer was examined in detail. The sample was structured as 10-nm Pt / 15-nm Ag /8-nm SiO_2 / p-type Si substrate. Figure 5.4 is the image of fresh dot. The left side of the electrode is a Pt layer and the Ag layer is on the right side, overlapping under the right side of Pt layer. We placed a probe electrode on the Pt side. Strong luminescence was observed in the overlapping area, while Ag–only-layer shows relatively weak luminescence, as shown in the Figure 5.5. Green light emission corresponds to 521 nm and 547 nm neutral Ag atomic lines. This result illustrates the effect of additional Pt layer, which enhances electrode connectivity even after the burst of explosion of electrode, and eventually leads to the enhancement of luminescence.

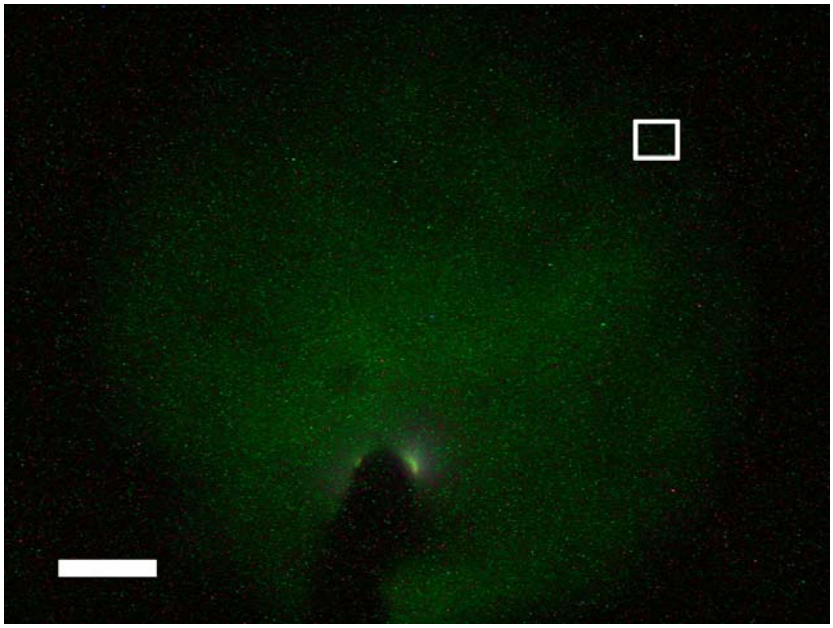

Figure 5.2 A micrograph of atomic luminescence from a Ag gate electrode (0.73 mm diameter) of a Si MOS structure under pulsed electrical excitation (accumulation of luminescence over 8 s with eight drives with a 60 V, 10 μs pulse with 1 s pulse interval), (scale bar, 100 μm)

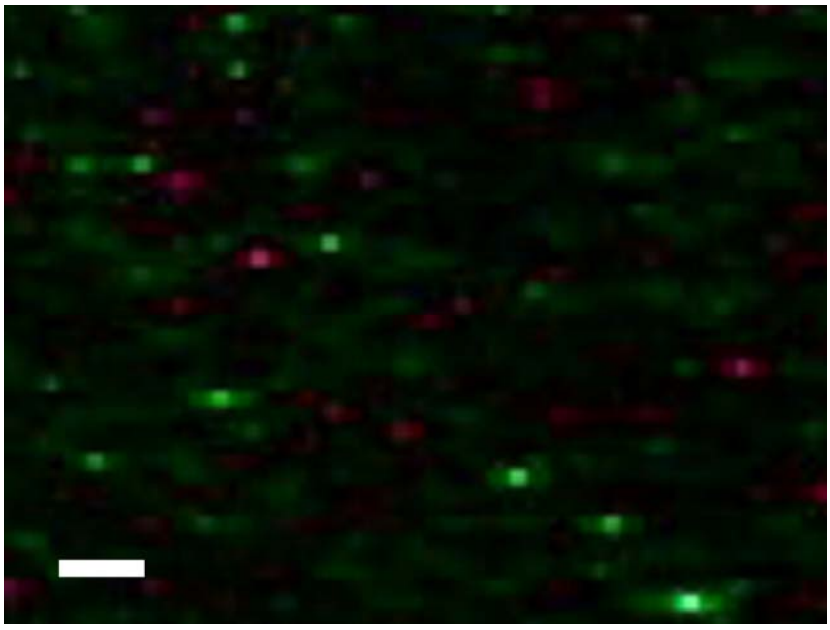

Figure 5.3 A magnified image of the squared area in Figure 5.2), (scale bar, 5 μm).

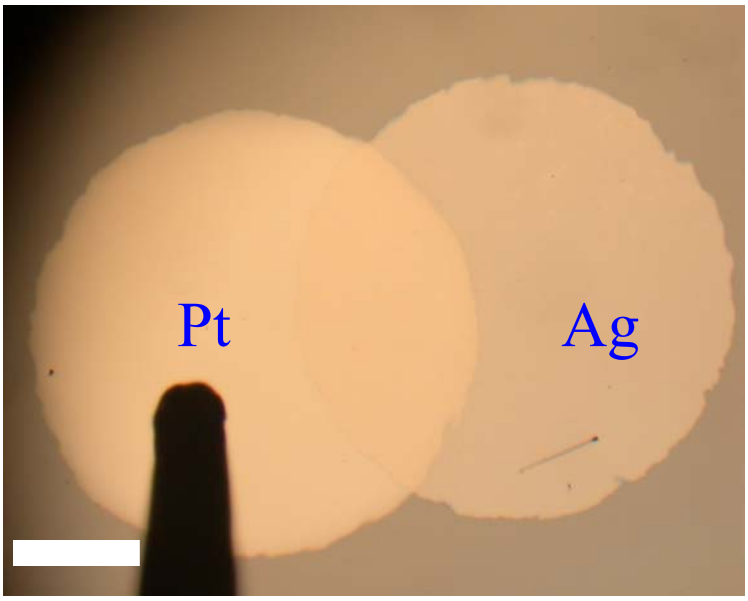

Figure 5.4 A fresh Pt and Ag overlapping electrode on SiO_2/ p-Si structure. (left) Pt layer, (right) Ag layer (scale bar, 200 μm)

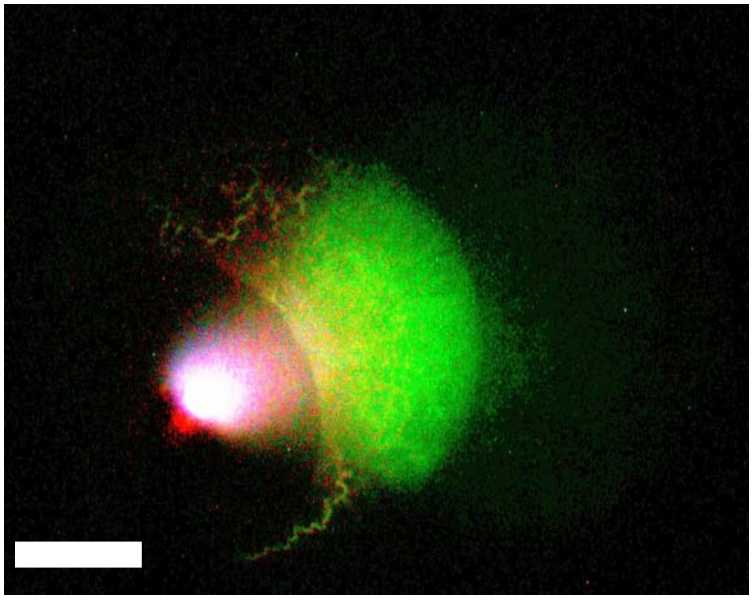

Figure 5.5 A micrograph of atomic luminescence from the Pt and Ag overlapping electrode on SiO_2/ p-Si structure under pulsed electrical excitation (accumulation of luminescence over 8 s with eight drives with a 100 V, 10 μs pulse with 1 s pulse interval) (scale bar, 200 μm)

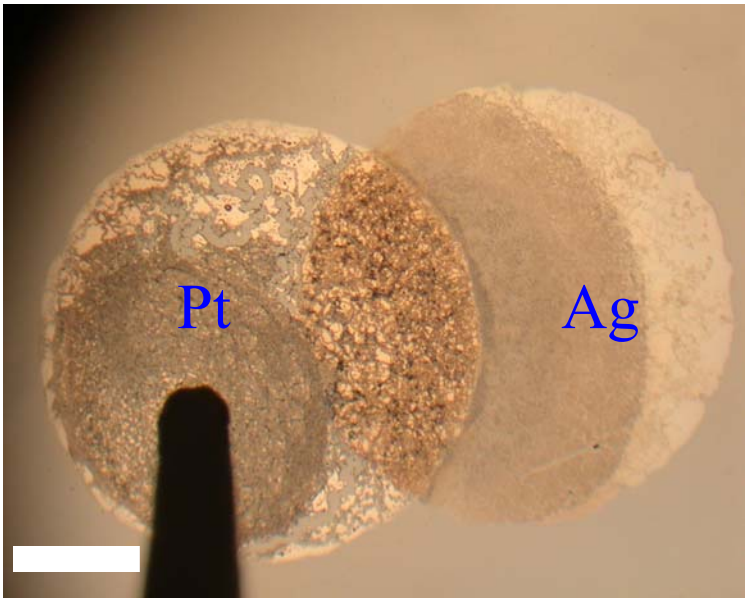

Figure 5.6 Deformed electrode after electrical excitation of the Pt and Ag overlapping electrode on SiO_2/ p-Si structure (scale bar, 200 μm)

5.3 OTHER ATOMIC SPECTRUM

A sample with a layered structure (Pt/SiN/Ag/SiN/SiO_2/p-type Si substrate) was tested. The base structure (SiO2/p-type Si substrate) was fabricated in the same steps as in Chapter 2. A 2-nm-thick SiN layer was then deposited with RF magnetron sputter deposition. A Si_3N_4 target (Angstrom Science, 3N purity) was used as a sputter source in nitrogen ambient. A 1-nm-Ag layer was deposited by thermal evaporation after the SiN layer deposition. Another 2-nm-SiN layer was deposited in the same way. For electrical contact on the front side, we deposited 10-nm-Pt layer by RF magnetron sputter deposition. −100 V and 10 ms pulse was applied to the gate.

Figure 5.7 shows the spectrum of atomic lines. The main peaks at 521 nm, 547 nm, 768 nm, and 827 nm are identified as the lines from neutral Ag atoms. The strong peaks at 413 nm, 506 nm, 589 nm, 598 nm, and 634 nm are from singly ionized Si atoms. Less strong, but clear lines are from neutral oxygen and neutral nitrogen are also observed.

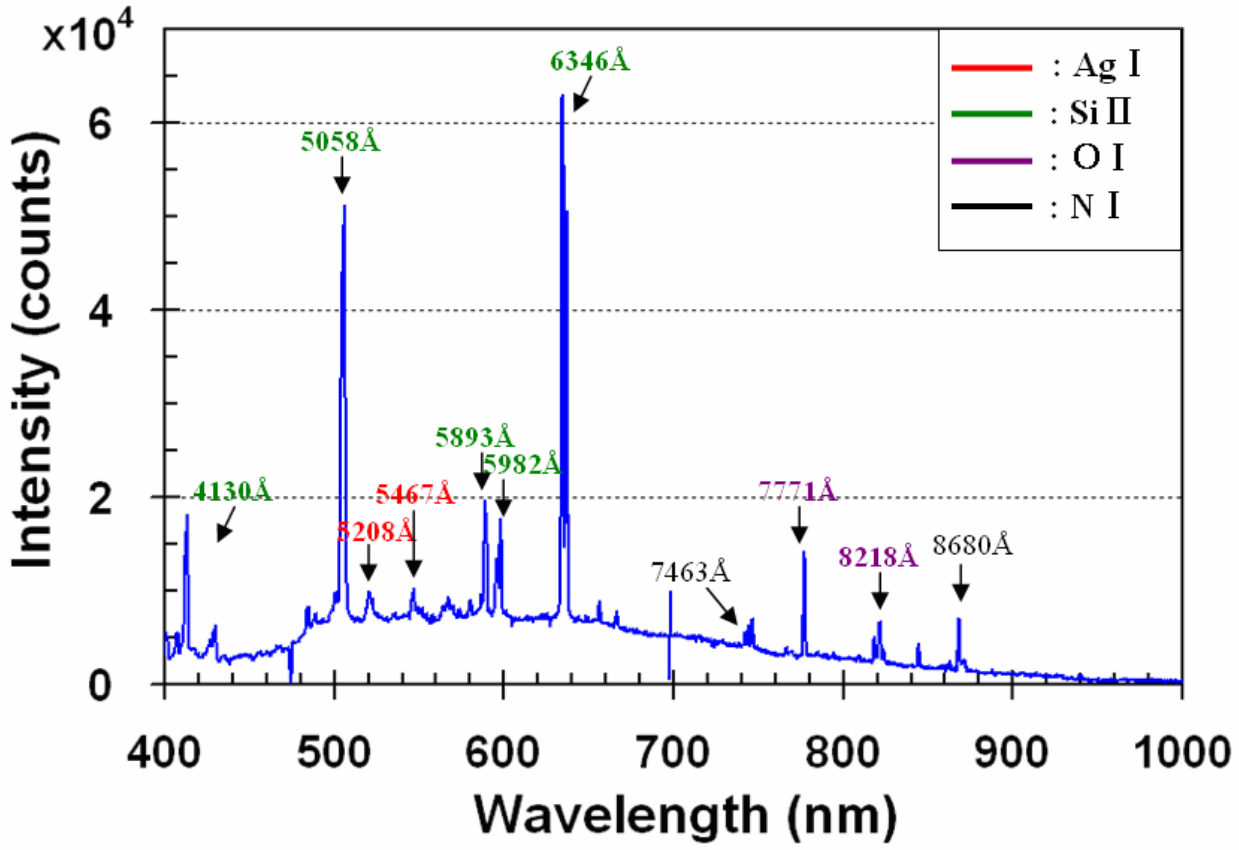

Figure 5.7. Luminescence spectra from a Si MOS structure (15-nm-thick Pt/2-nm SiN/1-nm Ag/2-nm SiN/ 8-nm-thick SiO_2 / p-type Si substrate) under negative voltage pulses (100 V amplitude; 10 ms width) applied to the gate

.

5.4 DISCUSSION

We observed strong atomic luminescence from a MOS structure under a pulse drive at both positive and negative voltage, ±100 V. The main peaks at 328 nm, 338 nm, 521 nm, 547 nm, 768 nm, and 827 nm are identified as atomic lines of neutral Ag atoms. From the microscopic image of luminescence, the distribution of luminescence centers is found to be relatively uniform. Finally, observation of atomic luminescence from other materials incorporated into the MOS structure demonstrates its potential as a simple method for element analysis.

6.0 SUMMARY AND CONCLUSIONS

In this thesis, we have investigated several phenomena involved in a MOS structure under pulse drive into a breakdown regime; ballistic transport in insulator, Coulomb explosion induced by highly kinetic electron impact ionization, and the resulting atomic luminescence. The base structure is a MOS capacitor (10~15 nm Ag / 8~10 nm SiO2 / p-type Si substrate). Applying a high voltage pulse (>10^8 V/ cm^2) at the gate, the luminescence and the *I-V* characteristic were measured. One of the essential aspects discovered in this study is the ballistic transport of carriers through SiO_2. It is known to be difficult to achieve a ballistic transport of electrons in a MOS structure with oxide thicker than 4 nm [14]. However, after a breakdown-process of oxide, it becomes possible mainly due to the formation of nano-channels in the oxide [23]. The *I-V* characteristic of the MOS structure reveals the current transport mechanism through the nano-channels to be the Child space-charge-limited current. This result suggests that the nano-channels in the oxide, formed after breakdown, are to work as collision-free paths for electrons. In the thick insulator case (thicker than a mean-free path for electron, 4 nm), the governing mechanisms of electrons transport at high electric field is the Mott-Gurney space-charge-limited current. Electrons cannot acquire high enough kinetic energy due to collisions with atoms on the path. However, nano-channels appear to provide a collision –free paths for electrons, so that they can attain high kinetic energy at the metal/SiO_2 interface.

In Chapter 4, another important phenomenon was discussed, which is Coulomb explosion by electron impact ionization. Coulomb explosion of atoms occurs when the Coulomb repulsion energy is higher than the binding energy of atoms. When the ballistic electrons hit the metal surface, the metal atoms can be impact ionized. When a sufficient number of ions accumulate in a given dimension, the system can be broken apart by electrostatic repulsion. Our experimental results show several evidences of Coulomb explosion. The first evidence is the atomic luminescence of Ag electrode, which indicates atomization, and excitation during the Coulomb explosion, and subsequent relaxation that produces luminescence. To meet the criteria of Coulomb explosion by electron impact ionization, sufficient current density should be acquired, which estimated to be > 10^8 A/cm^2 by calculation. Our current density measurement (~5x10^8 A/cm^2) is proved to be greater than the threshold level, satisfying one of the critical requirements. Lastly, electrode deformation pattern after application of a high voltage pulse supports Coulomb explosion. By comparison of the cases of applying pulse of 10 μs width and 10 ms width, it is found that crater-like deformation occurs in the initial stage of pulse drive, whereas melt-deformation is observed during post explosion period of the pulse. A consequential atomic luminescence was dealt with in Chapter 5. The main luminescence is identified as atomic luminescence of silver by examining the spectrum.

For further understanding of the findings of this study, several experiments are desired to be conducted. First, atomic force microscopy (AFM) in current conduction mode would be greatly helpful to confirm the formation of nano-channels. Secondly, the effect of reducing the oxide thickness should be investigated for the possibility of lower voltage operation. Finally, from the application point of view, the possibility of chemical analysis in our sample should be examined. Since Coulomb explosion produces secondary atomization, by simple deposition of

analyte on the Ag electrode, simple analysis of chemical components should be possible. The experiment with the sample (Pt/SiN/Ag/SiN/SiO2/p-type Si) in Chapter 5 shows its potential for elemental analysis.

REFERENCES

[1] N. Bohr and J. A. Wheeler, "The mechanism of nuclear fission" Phys. Rev. 56, 426-450 (1939).

[2] K. Sattler, J. Mühlbach, O. Echt, P. Pfau & E. Recknagel, "Evidence for Coulomb explosion of doubly charged microclusters" Phys. Rev. Lett. 47, 160-163 (1981).

[3] K. Codling and L. J. Frasinski, "Coulomb explosion of simple molecules in intense laser fields" Contemp. Phys. 35, 243-255 (1994).

[4] T. Ditmire, J. W. G. Tisch, E. Springate, M. B. Mason, N. Hay, R. A. Smith, J. Marangos & M. H. R. Hutchinson, "High-energy ions produced in explosions of superheated atomic clusters" Nature 386, 54-56 (1997).

[5] L. Köller, M. Schumacher, J. Köhn, S. Teuber, J. Tiggesbäumker & K. H. Meiwes-Broer, "Plasmon-enhanced multi-ionization of small metal clusters in strong femtosecond laser fields" Phys. Rev. Lett. 82, 3783-3786 (1999).

[6] D. Duft, T. Achtzehn, R. Müller, B. A. Huber & T. Leisner, "Rayleigh jets from levitated microdroplets" Nature 421, 128 (2003).

[7] F. Calvo, "Role of charge localization on the Coulomb fragmentation of large metal clusters: a model study" Phys. Rev. A 74, 043202 (2006).

[8] Z. Vager, R. Naaman & E. P. Kanter, "Coulomb explosion imaging of small molecules" Science 244, 426-431 (1989).

[9] A. G. Shenstone, "The arc spectrum of silver" Phys. Rev. 57, 894-898 (1940).

[10] A. G. Shenstone, "The spark spectrum of silver (Ag II)" Phys. Rev. 31, 317-322 (1928).

[11] The NIST Basic Atomic Spectroscopic Data website at http://physics.nist.gov/PhysRefData/Handbook/Tables/silvertable1.htm

[12] B. G. Streetman, S. Banerjee, *Solid State Electronic Device (5th Ed.)*, New York: Prentice Hall (2000).

[13] S. M. Sze, *Physics of Semiconductor Devices (2nd Ed)* New York: Wiley, 1981.

[14] Y. Y. Zhu, Z. B. Fang, S. Chen, C. Liao, Y.Q. Wu, Y.L. Fan and Z. M. Jiang, "Fowler-Nordheim hole tunneling in metal-Er_2O_3-silicon structures" Appl. Phys. Lett. 91, 122914(1)-(3) (2007).

[15] K. F. Schuegraf and C. Hu, "Hole Injection SiO_2 Breakdown Model for Very Low Voltage Lifetime Extrapolation" IEEE Trans. Electron devices, 41, 761-767 (1994).

[16] M. Lenzlinger and E. H. Snow, "Fowler-Nordheim tunneling into thermally grown SiO_2." J. Appl. Phys. 40, 278-283 (1969).

[17] N. M. Ravindra and J. Zhao, "Fowler-Nordheim tunneling in thin SiO_2 films" Smart Mater. Struct. 1, 197-201 (1992).

[18] H. Tanaka, "Limitation current in Si_3N_4/SiO_2 stacked dielectric films" Appl. Surf. Sci. 147, 222-227 (1999).

[19] Y. Feng, and J. P. Verboncoeur, "Transition from Fowler-Nordheim field emission to space charge limited current density" Phys. Rev. 97, 1538-1544 (2006).

[20] I. Langmuir, "The Effect of Space Charg and Residual Gases on Thermionic Current in High Vacuum" Phys. Rev. (Series 2) 2, 450-486 (1913).

[21] C. D. Child, "Discharge from Hot CAO"Phys. Rev. (Series 1) 32, 492-511 (1911).

[22] R. L. Liboff, *Introductory Quantum Mechanics (4th Ed)*, San Francisco: Addison Wesley (2003)

[23] D. J. DiMaria and J. H. Stathis "Ultimate limit for defect generation in ultra-thin silicon dioxide" Appl. Phys. Lett. 71, 3230-3232 (1997).

[24] S. Lombardo, A. La Magna, C. Spinella, C. Gerardi & F. Crupi, "Degradation and hard breakdown transient of thin gate oxides in metal-SiO_2-Si capacitors: dependence on oxide thickness" J. Appl. Phys. 86, 6382 (1999).

[25] F. A. Ilkov, J. E. Decker, S. L. Chin, "Ionization of atoms in the tunneling regime with experimental evidence using Hg atoms" J. Phys. B. 25, 4005-4020 (1992).

[26] A. A. Dakhel, "Poole-Frenkel electrical conduction in europium oxide films deposited on Si(100)" Cryst. Res. Technol. 38, 968-973 (2003).

[27] J. G. Simmons, "Poole-Frenkel Effect and Schottky Effect in Metal-Insulator-Metal Systems" Phys. Rev. 155, 657-660 (1967).

[28] A. Rose, “Space-charge-limited currents in solids” Phys. Rev. 97, 1538-1544 (1955).

[29] H. T. Henderson and K. L. Ashley, “Spece-Charge-Limited Current in Neutron-Irradiated Silicon, with Evidence of the Complete Lampert Triangle” Phys. Rev. 186, 811-815 (1969).

[30] M. Protopapas, C. H. Keitel & P. L. Knight, “Atomic physics with super-high intensity lasers” Rep. Prog. Phys. 60, 389-486 (1997).

[31] I. C. Chen, S. Holland, K. K. Young, C. Chang & C. Hu, “Substrate hole current and oxide breakdown” Appl. Phys. Lett. 49, 669 (1986).

[32] D. J. DiMaria, E. Cartier & D. Arnold, “Impact ionization, trap creation, degradation, and breakdown in silicon dioxide films on silicon” J. Appl. Phys. 73, 3367-3384 (1993).

[33] H. S. W. Massey, H. S. W. and D. R. Bates, D. R. “The properties of neutral and ionized atomic oxygen and their influence on the upper atmosphere” Rep. Prog. Phys. 9, 62-74 (1942).

[34] W. G. Graham, W. Fritsch, Y. Hahn & J. A. Tanis, ed., *Recombination of Atomic Ions” NATO ASI Series B: Phys. Vol 296*, New York: Plenum, 1992.

[35] R. H. M. Groeneveld, R. Sprik & A. Lagendijk, “Effect of a nonthermal electron distribution on the electron-phonon energy relaxation process in noble metals” Phys. Rev. B, 45, 5079-5082 (1992).

[36] R. Poirier and J. Olivier, “Energy losses of hot electrons in a thin layer of SiO_2 on Si” Appl. Phys. Lett. 21, 334-335 (1972).

[37] R. S. Freund, R. C. Wetzel, R. J. Shul & T. R. Hayes, “Cross-section measurements for electron-impact ionization of atoms” Phys. Rev. A, 41, 3575-3595 (1990).

[38] C. Jackschath, I. Rabin & W. Schulze, “Electron impact ionization of silver clusters Ag_n, $n \leq 36$” Z. Phys. D 22, 517-520 (1992).

[39] D. G. Vlachos, L. D. Schmidt & R. Aris, “Comparison of small metal clusters: Ni, Pd, Pt, Cu, Ag, Au” Supplement to Z. Phys. D 26, S156-158 (1993).

[40] L. Quaglia and C. Cornaggia, “Experimental Evidence of Excited Multicharged Atomic Fragments Coming from Laser-Induce Coulomb Explosion of Molecules” Phys. Rev. Lett. 84, 4565-4568 (2000).

[41] T. N. Theis, D. J. DiMaria, J. R. Kirtley & D. W. Dong, “Strong electric field heating of conduction-band electrons in SiO_2” Phys. Rev. Lett., 52, 1445-1448 (1984).

[42] M. V. Fischetti, "Monte Carlo solution to the problem of high-field electron heating in SiO_2" Phys. Rev. Lett. 53, 1755-1758 (1984).

[43] N. Klein and E. Burstein, "Electrical pulse breakdown of silicon oxide films" J. Appl. Phys. 40, 2728-2740 (1969).

[44] A. Bhattacharyya, "the leakage current in an $SiO_2/Si_3N_4/SiO_2$ interpoly dielectric layer in EPROM devices" J. Phys. D 21, 1287-1290 (1988).

[45] S. P. Wainwright and S. Hall, "Interpretation of high-field current-voltage and breakdown characteristics in SOI substrates formed using SIMOX technology" Semicond. Sci. Technol. 8, 1854-1856 (1993).

[46] M. Nafńa, J. Suné, and X. Avmerich, "Exploratory observations of post-breakdown conduction in polycrystalline-silicon and metal-gated thin-oxide metal-oxide-semiconductor capacitors" J. Appl. Phys. 73, 205-215 (1993).

[47] Rayleigh, Lord, "On the equilibrium of liquid conducting masses charged with electricity" Phil. Mag. 14, 184-186 (1882).

[48] L.V. Keldysh, "Ionization in the Field of a Strong Electromagnetic Wave" Sov. Phys. JETP 20, 1307-1314 (1965).